CHALMERS
UNIVERSITY OF TECHNOLOGY

Impact of Coulomb exchange interaction on exciton diffusion in 2D materials

Master of Nanotechnology

MARNE VERJANS

Department of Physics
CHALMERS UNIVERSITY OF TECHNOLOGY
Gothenburg, Sweden 2021

Master's thesis 2021:NN

Impact of Coulomb exchange interaction on exciton diffusion in 2D materials

MARNE VERJANS

CHALMERS
UNIVERSITY OF TECHNOLOGY

Department of Physics
Division of Condensed Matter and Materials Theory
Malic group
Chalmers University of Technology
Gothenburg, Sweden 2021

Impact of Coulomb exchange interaction on exciton diffusion in 2D materials
MARNE VERJANS

Supervisor: Ermin Malic, Department of Physics
Examiner: Ermin Malic, Department of Physics

Master's Thesis 2021
Department of Physics
Division of Condensed Matter and Materials Theory
Nanoscale quantum dynamics group
Chalmers University of Technology
SE-412 96 Gothenburg
Telephone +46 31 772 1000

Typeset in LaTeX
Printed by Chalmers Reproservice
Gothenburg, Sweden 2021

Impact of Coulomb exchange interaction exciton diffusion in 2D materials

MARNE VERJANS
Department of Physics
Chalmers University of Technology

Abstract

Transition metal dichalcogenides (TMDs) are a promising class of materials for future technologies due to their remarkable optical and electronic properties. In contrast to their bulk form, monolayer TMDs are direct bandgap semiconductors, which makes them promising candidates for optoelectronic devices. Furthermore, their atomically thin structure implies a reduced dielectric screening, resulting in a pronounced Coulomb interaction. This creates strongly bound electron-hole pairs, called excitons. These excitons can interact in many ways, which accounts for the rich exciton physics observed in monolayer TMDs. One example of possible interaction is the Coulomb exchange coupling. In this process, an exciton in the K valley is exchanged with an exciton in the K' valley and vice versa. It has been shown that the exchange coupling results in the entangling of K and K' excitons, creating a novel excitonic band geometry.
In this thesis we use the framework of density matrix theory to investigate the impact of the exchange coupling on exciton-phonon interaction and exciton diffusion in TMDs and in particular MoSe2. Moreover, we generalise the band geometry to include a detuning, e.g. induced by a magnetic field, and study how this changes the impact of Coulomb exchange coupling. We find that the exciton-phonon coupling becomes dependent on excitonic phase and exciton momentum. Furthermore, we reveal that the momentum-resolved exciton-phonon scattering rates show new scattering channels arising from the modified band geometry. Finally, the knowledge of the excitonic band structure and exciton-phonon scattering rates is used to calculate excitonic diffusion. We find that the diffusion coefficient can be controlled with a magnetic field-induced detuning of K and K' exciton states.

Acknowledgements

First of all I want to give sepcial thanks to Ermin and Samuel for giving me the opportunity to do this thesis and guiding and helping all these months.

I also want to thank Beatriz, Daniel, David, Joakim, Josh, Jamie, Maja, Raul and Roberto for their friendship and help during these days. It has been a pleasure to work together!

Thirdly, I a want to thank all the people from my church, with special thanks to Mats and Sandra, Gottfridssons family, Ferreiras family, Lindrens family, Sammy and Anne, Heitor and Celia, João Henrique and Hugo for helping me in difficult times and giving me all the support and friendship I so hard needed.

Also my parents I want to thank, for their support the past years and the sustaining me in everything I needed.
Lastly, I want to thank my Lord and God Jesus Christ for the new life I have through Him. This work is to His honour.

Marne Verjans, Gothenburg, October 2020

Contents

List of Figures

1

Introduction

Transition metal dichalcogenides (TMDs), known by the chemical formula MX_2, are semiconducting materials consisting of a transition metal M, e.g. W or Mo, and two chalcogen atoms X, e.g. Se or S. TMDs have been known for a long time, going all the way back to 1923, when their crystal structure was determined [1]. Most of these materials exhibit a layered structure held together by Van der Waals forces. With the advent of graphene in 2004, a bunch of atomically thin materials have been discovered. Due to their layered and well-studied structure, TMDs became the first materials after graphene to be produced in monolayers. In the following we will introduce some important concepts of TMDs that are important for this work.

1.1 TMD lattice

Figure 1.1a shows the crystal structure of a TMD monolayer. Like graphene, TMDs have a honeycomb lattice with two sublattices: one for the metal atoms (blue) and one with chalcogen atoms (green). The lattice has a unit cell spanned by the fundamental lattice vectors R_1 and R_2, which allows all lattice vectors to be expressed as $\mathbf{R} = n_1\mathbf{R_1} + n_2\mathbf{R_2}$, with n_1 and n_2 integers. In contrast to graphene, TMDs also have an out-of-plane structure, shown in Figure 1.1b, with lattice constant d_0. The TMD lattice is symmetric under three-fold rotations and in-plane mirror symmetry. However, the TMD lattice lacks inversion symmetry, which is an important difference with graphene.

The TMD Brillouin zone is given in Figure 1.1c. In this thesis, we will focus on the high-symmetry points of the first Brillouin zone, refferred to as K- and K' points. At these points, the valence band has a global maximum and the conduction band has a global minimum. Note that the K and K' points are related by time-reversal symmetry. The Brillouin zone principal lattice vectors are g_1 and g_2. With these, one can construct a general reciprocal lattice vector $\mathbf{G} = m_1\mathbf{g_1} + m_2\mathbf{g_2}$.

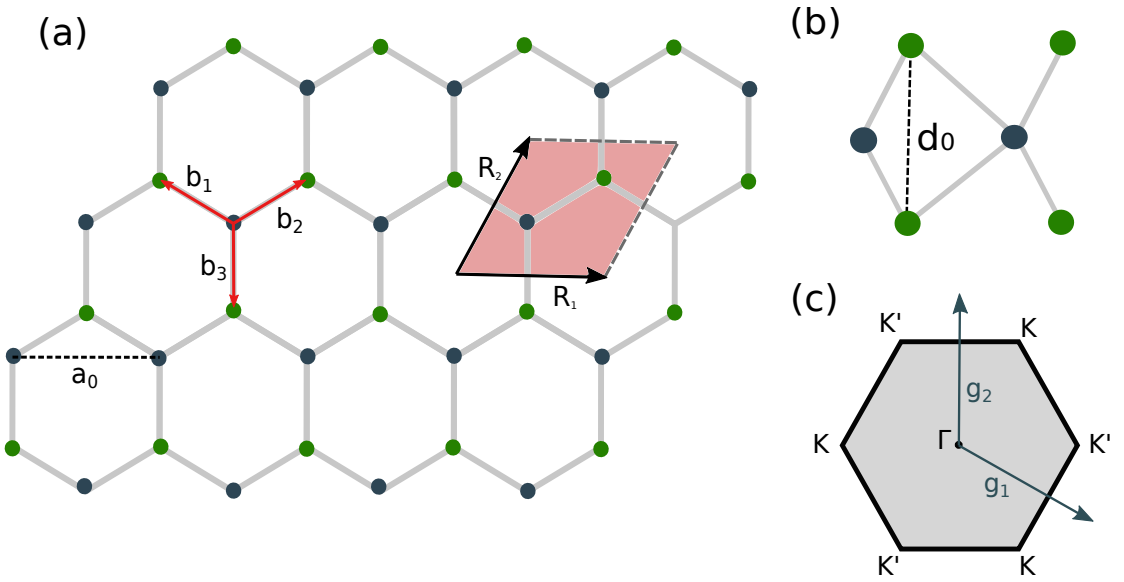

Figure 1.1: (a) Top view of TMD lattice with M atoms in blue and X in green. b_i denote the nearest neighbour vectors and a_0 the in-plane lattice constant. The unit cell is marked in red, spanned by the lattice vectors R_i. (b) TMD crossection with d_0 the out-of-plane lattice constant. (c) First Brillouin zone with high-symmetry points Γ and K/K'. Vectors $\mathbf{g_i}$ denote the principal reciprocal lattice vectors of the Brillouin zone.

1.2 Electronic Structure

The main contributions to the valence and conduction bands in TMDs come from the transition metal d-orbitals and chalcogen p-orbitals. The conduction band edge at the K and K' points knows a major contribution of the M-d_{z^2} orbital, whereas the valence band edge at the same points mainly consists of transition metal $d_{x^2-y^2}, d_{xy}$ orbitals. The chalcogen atoms give a minor contribution of p_x, p_y orbitals to both valence and conduction bands [2]. Besides, because of the three-fold rotational symmetry of the Billouin zone, the band structure in proximity of the high-symmetry points must be isotropic under rotational symmetry.

1.3 Optical Selection Rules and Spin-Valley Locking

An important consequence of the rotational and mirror symmetry of the lattice are the valley optical selection rules for TMDs [3, 4]. More specifically, the rotational symmetry determines the transitions between electronic bands that are allowed. Further, the mirror symmetry tells which optical chirality belongs to each state. Considering these together, one obtains valley optical selection rules that dictate that optical transitions in the K(K') valley only happen by $\sigma_+(\sigma_-)$ circularly polarised light. [5]

Besides the valley optical selection rules, TMDs also exhibit a strong spin-orbit coupling (SOC) because of the transition metal d-orbitals. This results in a spin-splitting of the bands in the K/K' valleys, which is reversed in both valleys due to time-reversal symmetry. As he SOC is strongest in the valence band, resulting in a large spin-splitting, one can say that the spin is coupled to the valley index. As a consequence, the optical selection rules become spin-dependent. The resulting optical selection rules are shown in Figure 1.2a. For the work in this thesis only the lowest energy transitions are regarded. This allows us to simplify the band structure to the picture shown in Figure 1.2b.

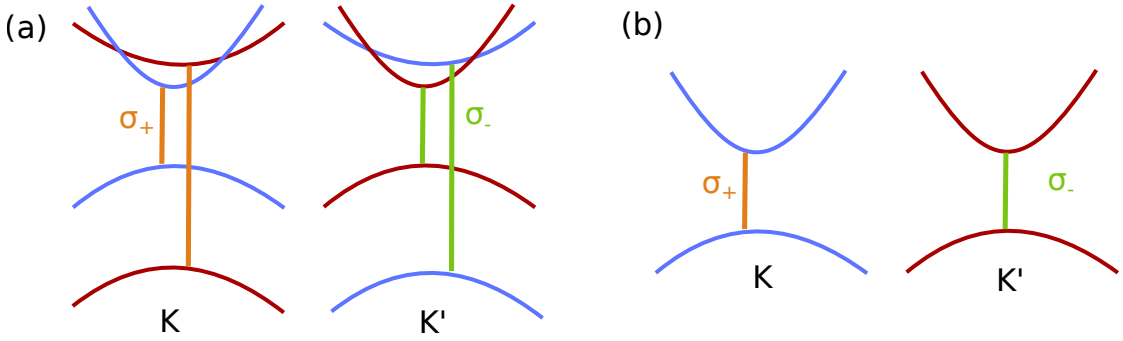

Figure 1.2: (a)Optical selection rules and spin-splitting for Mo based materials. Blue denotes spin up, red spin down. (b) Simplified picture used in this thesis.

1.4 Exchange coupling

Due to the strong Coulomb interaction, electrons in different high-symmetry points can interact. In particular, exchange interactions occur between electrons in the K/K' valleys, exhibiting an exchange of momentum. There are 10 possible exchange interactions in TMDs, from which 5 can be retrieved from time-reversal symmetry [6]. These are summarised in Figure 1.3. Different particle interactions are involved here. I and V denote electron exchange interactions, whereas III-IV denote electron-hole exchange interactions. This thesis focuses on process IV, i.e. the intervalley Coulomb exchange interaction. An analytical expression for it was calculated by Yu et al.[7], where they predicted that this interaction results in an effective coupling of the K and K' valleys. Also, they predicted that interaction of those excitons with linearly polarised light results in a spatially isotropic distribution of injected excitons, which can be experimentally verified by photoluminescence experiments. The goal of this work is to include phonons, i.e. quantised vibrations of the crystal lattice, and study the impact the of exchange coupling on the excitonic diffusion coefficient. Because the diffusion coefficient is a measurable quantity, this could provide an alternative way for verifying the presence and strength of the exchange coupling in TMDs.

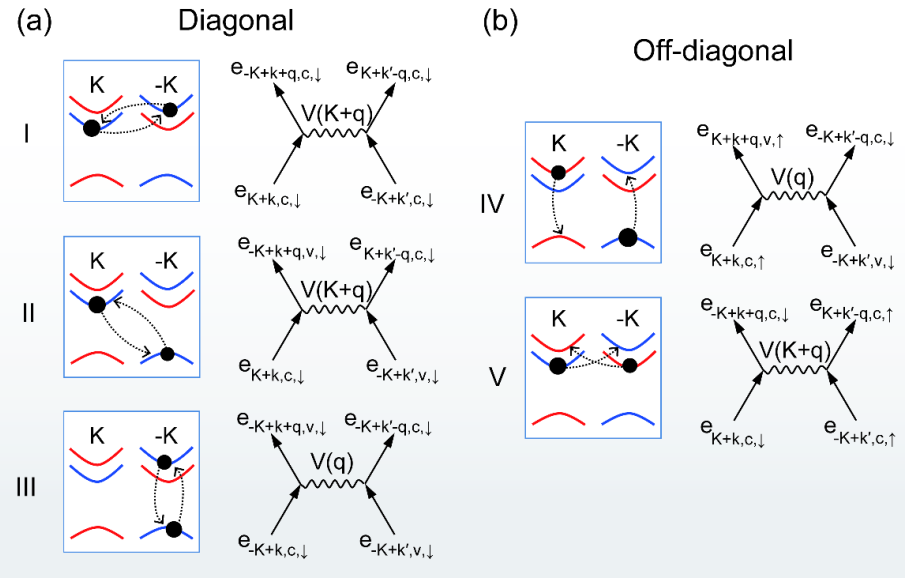

Figure 1.3: TMDs exhibit 5 different exchange interactions from which (a) 3 interactions exhibit no difference between in initial and final state. (b) 2 interactions result in a change in valley pseudo-spin. Figure taken from [6].

2

Theoretical Basics

2.1 Second Quantisation

The formalism of second quantisation or canonical quantisation is introduced in order to describe many-particle systems. Here follows a short summary of the formalism. In quantum mechanics there exist particles with integer spin, called Bosons, and with half-integer spin, called Fermions. An important property of these particles is their symmetry: N-particle Bosonic wave functions are always symmetric, N-particle Fermionic wave functions are always anti-symmetric. Due to the symmetry properties, a many-particle wavefunction can be fully described by its occupation number, together with a symmetrisation factor for permutations of the particles in the case of Fermions. Since a state only is described by symmetry and occupation number, the formalism can be simplified. therefore the Fock space is introduced, i.e. the subspace of Hilbert space whose states are defined by the occupation number and symmetry properties. A general N particle state is then represented as:

$$|n\rangle = |n_0, n_1, n_2, \ldots\rangle \,. \tag{2.1}$$

The state without any particles is called the "vacuum state" and is referred to as $|0\rangle$. The Fock states are incredibly useful in the sense that they allow to describe particle dynamics very easily. Indeed, using Fock states, it is easy to define so-called creation-annihilation operators, which add or destroy a particle in the N-particle state. The Bosonic creation-annihilation operators $b^\dagger, b$ are defined by their action on the N-particle state:

$$b_k^\dagger \,|n_0, n_1, \ldots, n_k, \ldots\rangle = \sqrt{n_k + 1}\,|n_0, n_1, \ldots, n_k + 1, \ldots\rangle \tag{2.2}$$
$$b_k \,|n_0, n_1, \ldots, n_k, \ldots\rangle = \sqrt{n_k}\,|n_0, n_1, \ldots, n_k - 1, \ldots\rangle \tag{2.3}$$

where $b_k^\dagger(b_k)$ creates (destroys) a particle at position k. The fundamental commutation relations for the Bosonic creation-annihilation operators read

$$[b_k, b_{k'}^\dagger] = \delta_{kk'}, \tag{2.4}$$
$$[b_k^\dagger, b_{k'}^\dagger] = [b_k, b_{k'}] = 0. \tag{2.5}$$

For the Fermionic operators $c^\dagger, c$, one needs to take into account the anti-symmetrisation of the wavefunction when defining creation-annihilation operators:

$$c_k^\dagger \left|\ldots, 0_k, \ldots\right\rangle = (-1)^{\sum_{i=1}^{k-1} n_i} \left|\ldots, 1_k, \ldots\right\rangle \tag{2.6}$$

$$c_k \left|\ldots, 1_k, \ldots\right\rangle = (-1)^{\sum_{i=1}^{k-1} n_i} \left|\ldots, 0_k, \ldots\right\rangle \tag{2.7}$$

$$c_k \left|\ldots, 0_k, \ldots\right\rangle = c_k^\dagger \left|\ldots, 1_k, \ldots\right\rangle = 0 \tag{2.8}$$

where the last equation comes from the Pauli exclusion principle. Due to the anti-symmetry property of Fermionic states, the Fermionic operators follow the anti-commutation relations

$$\{c_k, c_{k'}^\dagger\} = \delta_{kk'}, \tag{2.9}$$

$$\{c_k^\dagger, c_{k'}^\dagger\} = \{c_k, c_{k'}\} = 0. \tag{2.10}$$

Using the creation-annihilation operators, we can redefine the principle of wave function and introduce quantum field operators in real space:

$$\Psi^{(\dagger)}(\mathbf{r}) = \sum_\mu \psi_\mu^{(*)} a_\mu^{(\dagger)} \tag{2.11}$$

where ψ_μ are the wave functions from first quantisation. These field operators follow similar (anti-)commutation relations depending on the nature of the particle:

$$[\Psi(\mathbf{r_1}), \Psi^\dagger(\mathbf{r_2})] = \delta(\mathbf{r_1} - \mathbf{r_2}) \quad \text{Bosons} \tag{2.12}$$

$$\{\Psi(\mathbf{r_1}), \Psi^\dagger(\mathbf{r_2})\} = \delta(\mathbf{r_1} - \mathbf{r_2}) \quad \text{Fermions} \tag{2.13}$$

Lastly, we need an expression for general operators from first quantisation. Using the field operators, one finds that a single particle operators $\hat{A}^{(1)}$ are defined as

$$\hat{A}^{(1)} = \sum_{kk'} A_{kk'} a_k^\dagger a_{k'} \tag{2.14}$$

where the matrix element $A_{kk'} = \langle k' | \hat{A} | k \rangle$. A two-particle operator is defined as

$$\hat{A}^{(2)} = \sum_{k_1 k_2 k_3 k_4} A_{k_1 k_2}^{k_3 k_4} a_{k_4}^\dagger a_{k_3}^\dagger a_{k_2} a_{k_1} \tag{2.15}$$

with the matrix element $A_{k_1 k_2}^{k_3, k_4} = \langle k_3, k_4 | \hat{A} | k_1, k_2 \rangle$. For more information about second quantisation, read [8].

2.2 Density Matrix Formalism and Heisenberg Equations of Motion

The definition of the creation-annihilation operators in equations 2.2, 2.3 and 2.6, 2.7, relates to the number of particles in the state. This makes it convenient to define a density matrix $\rho_j^\lambda = \left\langle a_j^\dagger a_j \right\rangle$, which relates to the occupation probability of state i. The density matrix-formalism can be applied to electrons and phonons, with the carrier occupation probability of state k in band λ defined as $f_k^\lambda = \left\langle a_k^{\dagger\lambda} a_k^\lambda \right\rangle$ and the phonon occupation probability of mode α and momentum q defined as $n_q^\alpha = \left\langle b_q^{\dagger\alpha} a_q^\alpha \right\rangle$. Extending the formalism to off-diagonal terms, one can introduce the microscopic polarisation
$p_{kk'}^{\lambda\lambda'} = \left\langle a_k^{\dagger\lambda} a_{k'}^{\lambda'} \right\rangle$, which describes the coherence between carriers in different states and bands.
Within the field of quantum mechanics, two different but equivalent pictures co-exist: the Scrödinger picture and the Heisenberg picture. The former describes dynamics by the time evolution of the state vectors, given by the Schrödinger equation. In contrast, the latter uses time dependent operators to describe the system dynamics, described by the Heisenberg equation of motion. This allows us to describe the dynamics of any of the microscopic quantities that were introduced in this section. The Heisenberg equation of motion reads

$$i\hbar \frac{\partial \left\langle \hat{A} \right\rangle}{\partial t} = \left\langle [\hat{A}, \hat{H}] \right\rangle \tag{2.16}$$

where any operator in second quantisation (e.g. the microscopic polarisation) is represented by $\hat{A}$. The Heisenberg equation relates the time evolution of the operator to the commutator of $\hat{A}$ with the system Hamiltonian $\hat{H}$.
A downside of the Heisenberg equation is that it can give rise an infinite chain of coupled equations. Indeed, by taking a closer look at the equation, one observes that the time evolution of single particle operator depends on the system Hamiltonian, which can contain multi-particle interactions. Hence, also the equations of motion of the higher-order particle operators are needed to find a solution to the equation. In this way, one arrives at an infinite chain of coupled differential equations. The solution to this problem is to perform a correlation expansion, i.e. to truncate the system at finite order by assuming that higher orders are negligible [9]. The theory used in this work is based on the Hartree-Fock approximation, which approximates a two-particle quantity as

$$\left\langle a_i^\dagger a_j^\dagger a_k a_l \right\rangle = \left\langle a_i^\dagger a_l \right\rangle \left\langle a_j^\dagger a_k \right\rangle - \left\langle a_i^\dagger a_k \right\rangle \left\langle a_j^\dagger a_l \right\rangle + C_{kl}^{ij}, \tag{2.17}$$

where we assume that $C_{kl}^{ij} \approx 0$. This provides us with a useful tool to describe the motion of many-body systems at a microscopic scale.

3

System Hamiltonian

In quantum many body theory, the system Hamiltonian can be subdivided in energy contributions due to the interaction between all the particles of the system. In this thesis we consider interactions between electrons/holes and phonons. The system Hamiltonian is described as the sum of all interactions

$$\hat{H} = \hat{H}_{\text{free}} + \hat{H}_{\text{c-c}} + \hat{H}_{\text{c-p}}. \tag{3.1}$$

$\hat{H}_{\text{free}}$ describes the energy contributions of the free, non-interacting particles; $\hat{H}_{\text{c-c}}$ the two-particle carrier-carrier interaction and $\hat{H}_{\text{c-p}}$ the carrier-phonon interaction. In the following we will give a description of these Hamiltonians.

3.1 Free Particle Hamiltonian

The free particle Hamiltonian contains the contributions of non-interacting carriers and phonons. For the electronic Hamiltonian, we use the electronic operators a_l, where the compound index $l = (\lambda, \mathbf{k}, \xi, s)$ was introduced, with the λ the electronic band, $\mathbf{k}$ the electronic wave vector, ξ the valley pseudo-spin, and s the electron spin (which couples to the pseudo spin). Moreover, we treat the electronic energy in a parabolic approximation, i.e. the eigenenergy $\epsilon_l = E_l \pm \frac{\hbar^2 \mathbf{k}^2}{2m^l}$, with E_l the energetic separation from the Fermi level and m^l the effective electronic mass [10]. The free particle Hamiltonian is then expressed as

$$\hat{H}_{\text{c-free}} = \sum_l \epsilon_l a_l^\dagger a_l. \tag{3.2}$$

The dynamics of the crystal lattice is quantum mechanically described by phonons. These are quantised vibrations of the crystal lattice, which are treated as a quasi-particle. For describing phonons, we use the phonon operators $b_{\mathbf{q}}^\alpha$ with momentum $\mathbf{q}$. Different modes of phonons exist, which depend on the material. Generally, there exist acoustic and optical modes. The phonon mode index is given by α and the phonon eigenenergy for a specific mode and momentum we will define as $\omega_{\mathbf{q}}^\alpha$. The free phonon Hamiltonian can be derived by quantisation of the classical description of lattice vibrations, for which we refer to literature [9][10]. The free phonon Hamiltonian reads

$$\hat{H}_{\text{p-free}} = \sum_{\alpha\mathbf{q}} \omega_{\mathbf{q}}^\alpha (b_{\mathbf{q}}^{\dagger\alpha} b_{\mathbf{q}}^\alpha + \frac{1}{2}). \tag{3.3}$$

3.2 Carrier-carrier Hamiltonian

Electronic interactions are largely determined by the Coulomb interaction. We use the electronic operators λ, λ', where $\lambda = \{c, v\}$ to make a distinction between the electronic bands, i.e. the conduction band c and the valence band v. The Coulomb Hamiltonian reads [11, 12]:

$$\hat{H}_{\text{c-c}} = \frac{1}{2} \sum_{\lambda\lambda' \mathbf{k}\mathbf{k}'\mathbf{q} i i' j} V^{\lambda\lambda'}_{\mathbf{k}\mathbf{k}'\mathbf{q}} \lambda^{\dagger}_{\mathbf{k}+\mathbf{q}} \lambda'^{\dagger}_{\mathbf{k}'-\mathbf{q}} \lambda'_{\mathbf{k}'} \lambda_{\mathbf{k}} \tag{3.4}$$

where λ the band index. The Coulomb matrix element is defined as $V^{\lambda\lambda'}_{\mathbf{k}\mathbf{k}'\mathbf{q}} = V(\mathbf{q}) \mathcal{F}^{\lambda}_{\mathbf{k}}(\mathbf{q}) \mathcal{F}^{\lambda'}_{\mathbf{k}'}(-\mathbf{q})$, where the potential $V(\mathbf{q})$ denotes the Fourier transform of the Coulomb potential and $\mathcal{F}^{\lambda}_{\mathbf{k}}(\mathbf{q})$ is the form factor, defined as $\mathcal{F}^{\lambda}_{\mathbf{k}}(\mathbf{q}) = \langle \lambda, \mathbf{k}+\mathbf{q} | \, e^{i\mathbf{q}\cdot\mathbf{r}} \, | \lambda, \mathbf{k} \rangle$. An example of how this is treated in TMDs is found in the derivation of the Coulomb exchange coupling (Appendix A).
The electron-phonon Hamiltonian is given by [11] [12]

$$\hat{H}_{c-phon} = \sum_{\mathbf{k}\mathbf{q}\lambda\lambda'\alpha} D^{\lambda\xi\xi'\alpha}_{\mathbf{k},\mathbf{q}} \lambda^{\dagger\xi}_{\mathbf{k}+\mathbf{q}} \lambda^{\xi'}_{\mathbf{q}} (b^{\dagger\alpha}_{\mathbf{q}} + b^{\alpha}_{-\mathbf{q}}) \tag{3.5}$$

with $\mathcal{D}^{\xi\xi'}_{\alpha\mathbf{q}}$ the electron-phonon coupling, which reads

$$\mathcal{D}^{\xi\xi'}_{\alpha\mathbf{q}} = \sqrt{\frac{\hbar}{2\rho\omega^{\alpha}_{\mathbf{q}} A}} G^{\lambda\xi\xi'\alpha}_{\mathbf{k},\mathbf{q}}. \tag{3.6}$$

where ρ is the mass density of the unit cell. The deformation potential $G^{\lambda\lambda'\alpha}_{\mathbf{k},\mathbf{q}}$ depends on the derivative of the potential between electrons and ions [10]. In this work, only 5 phonon modes are relevant: the longitudinal and transverse acoustic modes (LA, TA) and longitudinal, transverse and out-of-plane optical modes (LO, TO, A1) [13]. For the acoustical phonons, the form factors are approximated by a first order effective deformation coupling $|G^{\lambda\xi\xi'\alpha}_{\mathbf{k},\mathbf{q}}| = D^{\lambda\Gamma\alpha}_{1} |\mathbf{q}|$ [14]. Optical phonons are approximated by a zeroth order deformation coupling $|G^{\lambda\xi\xi'\alpha}_{\mathbf{k},\mathbf{q}}| = D^{\lambda\Gamma\alpha}_{0}$ [10]. The values of these coefficient can be found in Appendix B.

3.3 Excitonic Hamiltonians

The electronic formalism as described before is very useful for describing single electronic properties of semiconductors. However, for describing excitonic phenomena, which are dominant in 2D materials, this becomes tedious. therefore, it is useful to redefine the formalism in an excitonic picture. We will use the semiconductor Bloch equations to derive the Wannier equation. This is the excitonic counterpart of the Schrödinger. The wave functions originating from the Wannier equation can then be used to create excitonic operators from the Fermionic operators used until now.

3.3.1 Semiconductor Bloch equations

The semiconductor Bloch equations of the microscopic polarisation $p^{\lambda\lambda'}_{\mathbf{k},\mathbf{k}'} = \left\langle a^{\dagger}_{\lambda\mathbf{k}} a_{\lambda'\mathbf{k}'} \right\rangle$ and the electronic occupation $f^{\lambda}_{\mathbf{k}} = \left\langle a^{\dagger}_{\lambda\mathbf{k}} a_{\lambda\mathbf{k}} \right\rangle$ describe the dy-

namics of electrons, holes and the optical polarisation near the semiconductor band gap [11]. The Heisenberg equation of motion of the microscopic polarisation reads

$$i\hbar\partial_t \left\langle a^\dagger_{\lambda\mathbf{k}} a_{\lambda'\mathbf{k}'} \right\rangle = \left\langle [a^\dagger_{\lambda\mathbf{k}} a_{\lambda\mathbf{k}'}, \hat{H}] \right\rangle \tag{3.7}$$

Using the definitions of the Hamiltonians and the fundamental commutation relations, one obtains the first semiconductor Bloch equation:

$$i\hbar\partial_t p^{\lambda\lambda'}_{\mathbf{k},\mathbf{k}'} = (\tilde{\epsilon}^{\lambda'}_{\mathbf{k}'} - \tilde{\epsilon}^{\lambda}_{\mathbf{k}}) p^{\lambda\lambda'}_{\mathbf{k},\mathbf{k}'} + (f^{\lambda'}_{\mathbf{k}'} - f^{\lambda}_{\mathbf{k}}) \tilde{\Omega}^{\lambda'\lambda}_{\mathbf{k},\mathbf{k}'}(t) \tag{3.8}$$

with the renormalised energies:

$$\tilde{\epsilon}^{\lambda}_{\mathbf{k}} = \epsilon^{\lambda}_{\mathbf{k}} + \sum_{\mathbf{q}} V^{\lambda\lambda}_{\mathbf{k}',\mathbf{k}'+\mathbf{q},\mathbf{q}} f^{\lambda}_{\mathbf{k}'+\mathbf{q}} \tag{3.9}$$

and Rabi frequency $\tilde{\Omega}^{\lambda'\lambda}_{\mathbf{k},\mathbf{k}'}(t)$.
From the Heisenberg equation of motion for the band occupation $f^{\lambda}_{\mathbf{k}} =< a^\dagger_{\mathbf{k}} a_{\mathbf{k}} >$ one finds the second semiconductor Bloch equation:

$$\hbar\partial_t f^{\lambda}_{\mathbf{k}} = \sum_{\lambda'\mathbf{k}'} Im\{(\tilde{\Omega}^{\lambda'\lambda}_{\mathbf{k},\mathbf{k}'})^* p^{\lambda\lambda'}_{\mathbf{k},\mathbf{k}'}\} \tag{3.10}$$

For a detailed derivation, see [11].

3.3.2 Wannier Equation

The Wannier equation describes the motion of joint electron-hole pairs, called excitons. The electron-hole motion is analogous to an atom, at which the electron is bound to the hole and "circles" around it in quantised energy levels. The equation can be derived from the semiconductor Bloch equations, see [11] [10]. This results in:

$$(\epsilon^{c}_{\mathbf{k_e}} - \epsilon^{v}_{\mathbf{k_h}})\Phi(\mathbf{k_e}, \mathbf{k_h}) - \sum_{\mathbf{l}} V_{\mathbf{k_e},\mathbf{k_h}+\mathbf{l},\mathbf{l}} \Phi(\mathbf{k_e}+\mathbf{l}, \mathbf{k_h}+\mathbf{l}) = E^{ex}_{\mathbf{k_e},\mathbf{k_h}} \Phi(\mathbf{k_e}, \mathbf{k_h}), \tag{3.11}$$

where $\mathbf{l}$ represents momentum and $E^{ex}_{\mathbf{k_e},\mathbf{k_h}}$ the excitonic eigenenergy. Because the Wannier equation describes excitonic states, it is good to go to a joint coordinate systen for electrons and holes. By introducing the centre-mass momentum $\mathbf{Q}$ and relative momentum $\mathbf{q}$ defined as

$$\mathbf{Q} = \mathbf{k_e} - \mathbf{k_h} \tag{3.12}$$

$$\mathbf{q} = \alpha\mathbf{k_e} + \beta\mathbf{k_h} \tag{3.13}$$

with $\alpha = \frac{m_e}{m_e+m_h}$, $\beta = \frac{m_h}{m_e+m_h}$. In the end one arrives to the Wannier equation in excitonic basis

$$\frac{\hbar^2\mathbf{q}^2}{2m_r}\Psi^{\xi\mu}(\mathbf{q}) - \sum_{\mathbf{l}} V_{\mathbf{l}} \Psi^{\xi\mu}(\mathbf{l}+\mathbf{q}) = E^{b}_{\mu}\Psi^{\xi\mu}(\mathbf{q}) \tag{3.14}$$

where $m_r = m_e^{-1} + m_h^{-1}$ is the relative mass and E_μ^b the excitonic binding energy. The indices μ and ξ represent the excitonic level (in this work always 1s) and the valley index, respectively.Further, we assumed here that
$\Phi(\mathbf{Q}, \mathbf{q}) = exp(i\theta^e_{\mathbf{q}+\alpha\mathbf{Q}} - i\theta^h_{\mathbf{q}-\beta\mathbf{Q}})\Psi(\mathbf{q})$, i.e. the wavefunctions are not dependent on the centre-of-mass momentum. Note that in this thesis, the dependence on the topological phase $\theta^\lambda_\mathbf{k}$ will be neglected. Finally, the equation of motion for the microscopic polarisation can be transformed into excitonic basis using the eigenfunctions from the Wannier equation, from which one obtains the excitonic eigenenergy

$$E^{\xi\mu}_\mathbf{Q} = \frac{\hbar^2\mathbf{Q}^2}{2M^\xi} + \Delta_\xi + E^b_\mu \tag{3.15}$$

with $M^\xi = m^\xi_e + m^\xi_h$ the excitonic mass in valley ξ and Δ_ξ the band gap. For the full derivation, see [12].

3.3.3 Excitonic Operators

The excitonic eigenstates $\Psi(\mathbf{q})$ from the Wannier equation can be used to construct excitonic creation and annihilation operators. This is a summary of the derivation in [12].
First we define pair operators

$$A^\dagger_{\mathbf{k}\mathbf{k}'} = e^\dagger_\mathbf{k} v_{\mathbf{k}'} \tag{3.16}$$

From the fundamental commutation relations for electron operators one finds commutation relations for exciton operators

$$[A_{\mathbf{k_1}\mathbf{k_2}}, A^\dagger_{\mathbf{k_3}\mathbf{k_4}}] = \delta_{\mathbf{k_1}\mathbf{k_3}}\delta_{\mathbf{k_2}\mathbf{k_4}} + v_{\mathbf{k_2}} v^\dagger_{\mathbf{k_4}}\delta_{\mathbf{k_1}\mathbf{k_3}} + c^\dagger_{\mathbf{k_3}} c_{\mathbf{k_1}}\delta_{\mathbf{k_2}\mathbf{k_4}} \tag{3.17}$$

$$\approx \delta_{\mathbf{k_1}\mathbf{k_3}}\delta_{\mathbf{k_2}\mathbf{k_4}} \tag{3.18}$$

The last step can be only done when assuming a low-excitation limit. These commutation relations can be used to rewrite the electron-hole commutation relation into excitonic operators, i.e.

$$c^\dagger_\mathbf{k} c_{\mathbf{k}'} = \sum_\mathbf{l} A^\dagger_{\mathbf{k}\mathbf{l}} A_{\mathbf{k}'\mathbf{l}} \tag{3.19}$$

$$v_\mathbf{k} v^\dagger_{\mathbf{k}'} = \sum_\mathbf{l} A^\dagger_{\mathbf{l}\mathbf{k}} A_{\mathbf{l}\mathbf{k}'} \tag{3.20}$$

In the end we can develop the pair operators in excitonic basis

$$A^\dagger_{\mathbf{k_e}\mathbf{k_h}} = \sum_{\xi\mu} X^{\dagger\xi\mu}_{\mathbf{k_e}-\mathbf{k_h}} \Psi^{\xi\mu}(\alpha_\xi \mathbf{k_h} + \beta_\xi \mathbf{k_e}) \tag{3.21}$$

3.3.4 Excitonic Hamiltonians

A simple illustration of how the transforming of the Hamiltonians works, can be found in the derivation of the exchange coupling element in Appendix A. Using these operators, the carrier-carrier Hamiltonian transforms to

$$\hat{H}_{x-0} = \sum_{\mathbf{Q}\xi} E^{\xi}_{\mathbf{Q}} X^{\dagger\xi}_{\mathbf{Q}} X^{\xi}_{\mathbf{Q}} \tag{3.22}$$

where E^{ξ} is the excitonic energy for the 1s state. The electron-phonon Hamiltonian transforms to

$$\hat{H}_{x-ph} = \sum_{\mathbf{Q}\mathbf{q}\xi\xi'\alpha} g^{\xi\xi'\alpha}_{\mathbf{Q}\mathbf{q}} X^{\dagger\xi'}_{\mathbf{Q}+\mathbf{q}} X^{\xi}_{\mathbf{Q}} (b_{\mathbf{q}} + b^{\dagger}_{\mathbf{q}}) \tag{3.23}$$

with the transformed exciton-phonon coupling $g^{\xi\xi'\alpha}_{\mathbf{Q}\mathbf{q}} = (g^{\xi\xi'\alpha}_{\mathbf{Q}\mathbf{q}})^c - (g^{\xi\xi'\alpha}_{\mathbf{Q}\mathbf{q}})^v$ and

$$(g^{\xi\xi'\alpha}_{\mathbf{Q}\mathbf{q}})^c = D^{\alpha c} \sum_{\mathbf{k}} \Psi^{*\xi}(\mathbf{k}) \Psi^{\xi'}(\mathbf{k} + \beta_{\xi}\mathbf{q}) \tag{3.24}$$

$$(g^{\xi\xi'\alpha}_{\mathbf{Q}\mathbf{q}})^v = D^{\alpha v} \sum_{\mathbf{k}} \Psi^{*\xi}(\mathbf{k}) \Psi^{\xi'}(\mathbf{k} - \alpha_{\xi}\mathbf{q}) \tag{3.25}$$

Here it was explicitly assumed that we only work with K/K' valleys and 1s excitons. Note further that the sign convention about these matrix elements is unclear [10]. For this reason we neglect crossing term when calculating $|g^{\xi\xi'\alpha}_{\mathbf{Q}\mathbf{q}}|^2$.

4

Coulomb Exchange Interaction

The main focus in this thesis will be to use the formalism of the excitonic Hamiltonian to study the electron-hole intervalley Coulomb exchange interaction, illustrated by Figure 4.1. The Feynman diagram describes how a valence electron in K exchanges the momentum q with a conduction electron in K'.

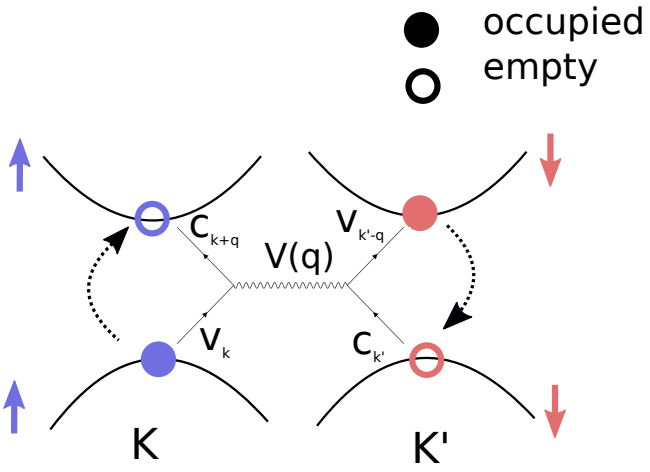

Figure 4.1: Schematic representation of the electron-hole exchange interaction with the corresponding Feynman diagram.

The intervalley exchange Hamiltonian in electronic picture reads

$$\hat{H}_{ex} = \sum_{\mathbf{k},\mathbf{k'},\mathbf{q}} \mathcal{J}_{ex}(\mathbf{k},\mathbf{k'},\mathbf{q}) c^{\dagger K}_{\mathbf{k+q}} v^{\dagger K'}_{\mathbf{k'-q}} c^{K'}_{\mathbf{k'}} v^{K}_{\mathbf{k}} + h.c. \tag{4.1}$$

where $\mathcal{J}_{ex}(\mathbf{k},\mathbf{k'},\mathbf{q})$ represents the exchange coupling strength, **k,k'** denote the initial electronic wave vectors and **q** denotes the momentum that is transferred by the exchange. Changing the coordinate system to joint electron-hole coordinates, the Hamiltonian can be written in excitonic picture (see appendix A.1):

$$\hat{H}_{ex} = \sum_{\mathbf{Q}} \mathcal{J}_{\mathbf{Q}} X^{\dagger K}_{\mathbf{Q}} X^{K'}_{\mathbf{Q}} + \text{h.c.} \tag{4.2}$$

with the transformed exchange coupling $\mathcal{J}^{\xi}_{\mathbf{Q}} = \sum_{\mathbf{kk'}} \psi_{-\mathbf{k}} \psi_{\mathbf{k'}} \mathcal{J}_{\mathbf{kk'q}}$ and $\psi_{\mathbf{k}}$ the excitonic wave functions.
From the optical selection rules and the spherical symmetry of the system, an analytical solution for the exchange coupling can be derived [3]:

$$\mathcal{J}_{\mathbf{Q}} = -\frac{|\sum_{\mathbf{q}} \psi_{\mathbf{q}}|^2}{A} \frac{a^2 t^2}{E_g^2} V(\mathbf{Q}) Q^2 e^{-2i\theta} \tag{4.3}$$

where A denotes the sheet area, a the lattice constant, t the hopping parameter, E_g the band gap and θ the excitonic phase, i.e. due to the rotational symmetry of the band structure, any momentum vector can be expressed as $\mathbf{Q} = (Q\cos\theta, Q\sin\theta)$. The detailed derivation of this expression is found in Appendix A. In order to account for the screening of electrons, the Rytova-Keldysh potential is used [15] [16] :

$$V(\mathbf{Q}) = \frac{e^2}{2\epsilon_0 \epsilon_{\mathrm{r}} A} \frac{1}{|\mathbf{Q}|(1 + r_0|\mathbf{Q}|)} \tag{4.4}$$

The Keldysh potential depends on the unit charge e, the vacuum permittivity ϵ_0, the dielectric constant of the substrate ϵ_{r} and the screening length r_0, defined by $r_0 = \frac{d_0 \epsilon_\perp}{\epsilon_r}$. d_0 represents the thickness of the monolayer and $\epsilon_\perp$ the out-of-plane dielectric constant. Note that the dependence on ϵ_r means that encapsulation of a monolayer can influence the exchange coupling. We will consider a freestanding monolayer ($\epsilon_r = 1$) and a monolayer of with hexagonal boron nitride (hBN) encapsulation ($\epsilon_r = 4.5$).
Having defined the exchange coupling, the complete Coulomb Hamiltonian reads:

$$\hat{H}_{x-0} = \sum_{\mathbf{Q}\xi} E_{\xi\mathbf{Q}} X_{\mathbf{Q}}^{\dagger\xi} X_{\mathbf{Q}}^{\xi} + \sum_{\mathbf{Q}} \mathcal{J}_{\mathbf{Q}} X_{\mathbf{Q}}^{\dagger K} X_{\mathbf{Q}}^{K'} + \text{h.c.}. \tag{4.5}$$

In order to determine the eigenstates and eigenenergies of the system, the Hamiltonian can be reduced to a matrix problem by introducing spinors:

$$X^K = \begin{pmatrix} 1 \\ 0 \end{pmatrix}, X^{K'} = \begin{pmatrix} 0 \\ 1 \end{pmatrix} \tag{4.6}$$

The Hamiltonian in this basis reads:

$$\hat{H}_{x-0,\mathbf{Q}} = \begin{pmatrix} E_{\mathbf{Q}}^K & \mathcal{J}_{\mathbf{Q}} \\ \mathcal{J}_{\mathbf{Q}}^* & E_{\mathbf{Q}}^{K'} \end{pmatrix} \tag{4.7}$$

Diagonalisation of the Hamiltonian matrix results in new eigenenergies $\widetilde{E}_{\mathbf{Q}}^{\sigma} = \frac{\hbar^2 Q^2}{M} + \sigma \mathcal{J}_{\mathbf{Q}}$. Here, the branch index σ was introduced, with $\sigma = -1$ for the lower branch and $\sigma = +1$ for the upper branch. The corresponding eigenbasis is given by

$$Y_{\mathbf{Q}}^{\sigma} = \frac{1}{\sqrt{2}}(X_{\mathbf{Q}}^K + \sigma e^{i2\theta} X_{\mathbf{Q}}^{K'}). \tag{4.8}$$

Next, the exciton Hamiltonian can be generalised for a detuning Δ, which can be induced by e.g. a perpendicular magnetic field. These terms will be considered equivalent in this thesis. In the uncoupled case, the detuning results in the splitting of the exciton bands s.t. $E_{\mathbf{Q}}^K = \frac{\hbar^2 Q^2}{M} - \Delta$, $E_{\mathbf{Q}}^{K'} = \frac{\hbar^2 Q^2}{M} + \Delta$. Following the same derivation as before, the eigenenergies of the coupled system become

$\widetilde{E}^{\sigma}_{\mathbf{Q}} = \frac{\hbar^2 Q^2}{M} + \sigma\sqrt{\Delta^2 + |\mathcal{J}_{\mathbf{Q}}|^2}$. Figure 4.2a,b shows the modified band structure for a freestanding and hBN encapsulated monolayer of $MoSe_2$. It is clear that the exchange coupling acts as a momentum-dependent splitting of the original parabolic dispersion.

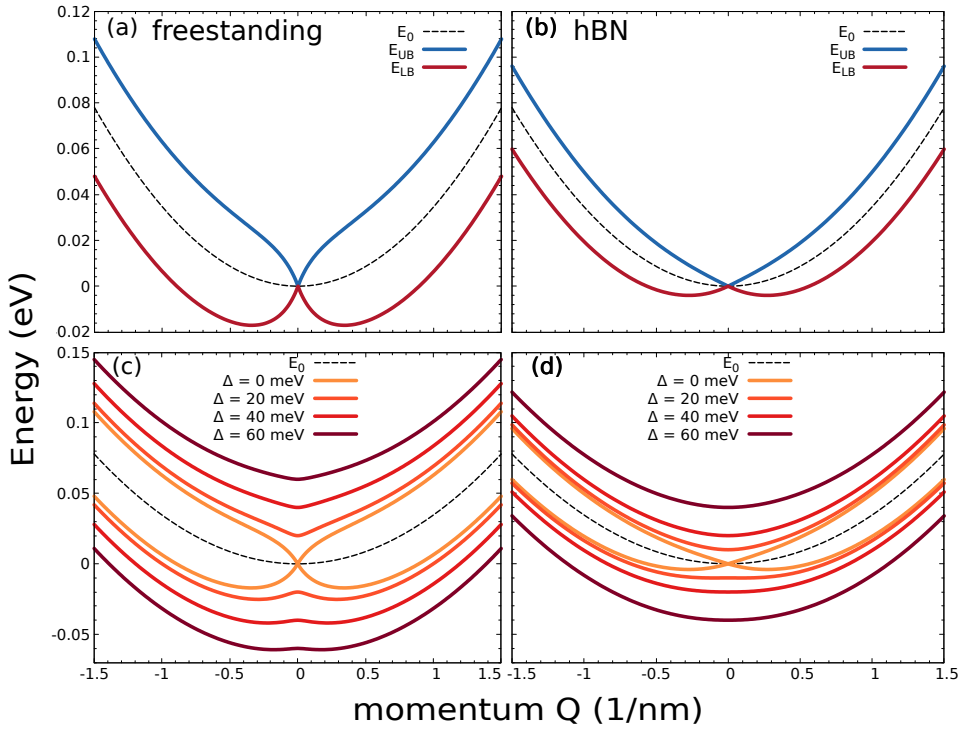

Figure 4.2: (a)-(b): excitonic band structure with exchange coupling for a freestanding and hBN encapsulated monolayer of MoSe2 respectively.(c)-(d): excitonic band structure for different detunings in a freestanding and hBN encapsulated monolayer of MoSe2 respectively.

At zero momentum, the band structure is degenerate as the lower and upper branches are equal. This results in a Dirac-like dispersion in the limit of small momenta. In this limit, the band structure can be approximated by $E^{\sigma}_{\mathbf{Q}} = \sigma J_0 Q$, with $J_0 = -\frac{|\sum_{\mathbf{q}} \psi_{\mathbf{q}}|^2}{A} \frac{a_0^2 t^2 e^2}{E_g^2} \frac{1}{2\epsilon_0 \epsilon_r}$. The slope of the curve depends on the inverse of the relative dielectric constant. This means that for a hBN encapsulated monolayer with $\epsilon_r = 4.5$, the exchange coupling is 4.5 times weaker than a freestanding monolayer. This explains the difference in splitting between Figures 4.2a and 4.2b. When momentum increases, the band structure takes on a parabolic shape. In the limit of $Q \to \infty$, the splitting becomes constant with $E^{\sigma}_{Q} = \frac{\hbar^2 Q^2}{2M} + \sigma \frac{J_0}{r_0}$.
In presence of a detuning, the band structure deforms. This is shown in Figures 4.2c,d. By taking the limiting case $\Delta >> \mathcal{J}_Q$, the branches should split by Δ. This implies that a magnetic field effectively decouples the K and K' valleys. The detuning pushes the local maximum down, deforming the branch to a parabola. The critical magnetic field Δ_0 at which this happens can be derived by taking the second derivative of the lower branch. One then finds $\Delta_0 = J_0^2 \frac{M}{\hbar^2}$. For a freestanding

monolayer this means that $\Delta_0 = 344$ meV. With hBN encapsulation this number reduces to $\Delta_0 = 14$ meV.

4.1 Bloch Sphere and Eigenstates

Due to the exchange coupling, excitons become a coherent superposition of the K and K' valleys, as we saw in equation 4.8. The phase factor contains a winding number 2, which means that the valley pseudospin rotates with 4π for one rotation in momentum space [6] [17]. This is illustrated in Figure 4.3. Note that this result is the same as in [6].

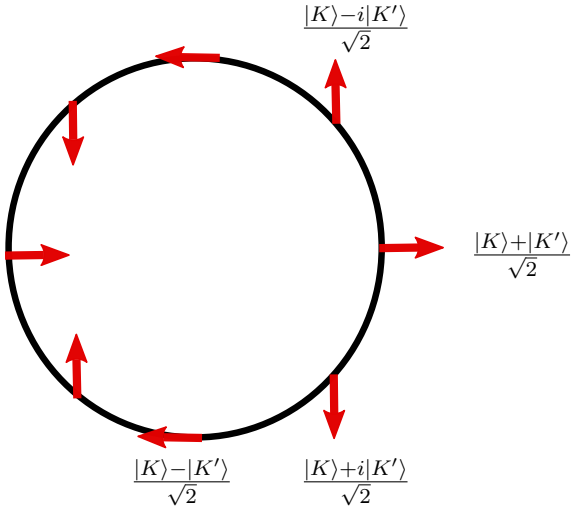

Figure 4.3: Crossection of the lower branch. Arrows denote the valley pseudospin. Figure inspired on [17].

Until now, the eigenstates with detuning remained undiscussed. They are given by

$$Y^{\sigma}_{\mathbf{Q}} = \frac{X^{K}_{\mathbf{Q}} + t^{\sigma}_{\mathbf{Q}} e^{i2\theta} X^{K'}_{\mathbf{Q}}}{\sqrt{1 + |t^{\sigma}_{\mathbf{Q}}|^2}}. \tag{4.9}$$

with $t^{\sigma}_{\mathbf{Q}} = \frac{\Delta + \sigma\sqrt{\Delta^2 + |\mathcal{J}_{\mathbf{Q}}|^2}}{|\mathcal{J}_{\mathbf{Q}}|}$. The best way to visualise the eigenstates is by using the Bloch sphere. A general state of a two-level system on the Bloch sphere is expressed by

$$|\psi\rangle = \cos\frac{\theta}{2}|K\rangle + \sin\frac{\theta}{2} e^{i\phi}|K'\rangle \tag{4.10}$$

with θ the azimuthal angle (not the mix up with the excitonic phase θ) and ϕ the in-plane phase. According to equation 4.8, the eigenstates in the absence of a detuning are a coherent superposition of K and K' states. The azimuthal angle $\theta = \frac{\pi}{2}$ is constant, so the states are located on the equator of the Bloch sphere. The phase ϕ is important for optical experiments, where the location on the equator determines the light polarisation [6], but will also play a role in scattering with phonons as will be shown in the next chapter.

In presence of a magnetic field, θ becomes

$$\theta = 2 \arccos \frac{1}{\sqrt{1 + |t^{\sigma}_{\mathbf{Q}}|^2}}. \tag{4.11}$$

The azimuthal angle is a measure for the proportion of the state mixture. It was noted that detuning results in a decoupling of the K and K' valleys. This means that for $\Delta >> \mathcal{J}_{\mathbf{Q}}$, $Y^0_{\mathbf{Q}} = X^K_{\mathbf{Q}}$, $Y^1_{\mathbf{Q}} = X^{K'}_{\mathbf{Q}}$. This is nicely reflected in the states on the Bloch sphere in Figure 4.4. Note that the states in Figure 4.3 correspond to rotations on the equator of the Bloch sphere.

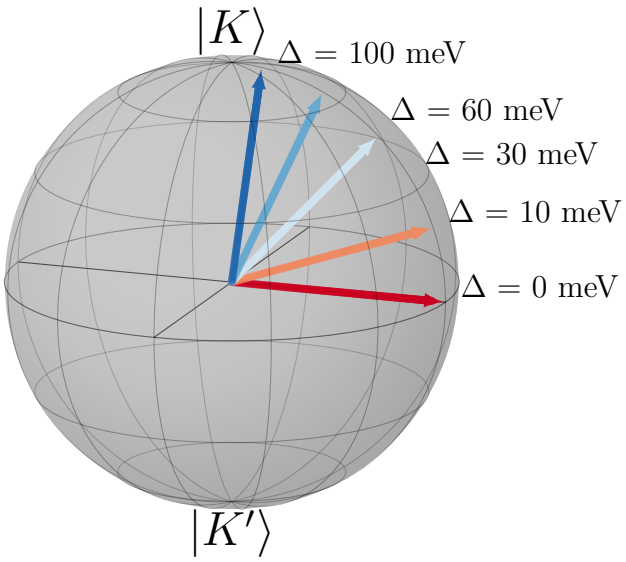

Figure 4.4: Eigenstates for the lower branch at $Q = 1$.

In presence of a magnetic field, the length of the eigenstates also depends of the exciton momentum. Figure 4.5a shows the proportion of K excitons in the eigenstates of the lower branch, denoted as $|U^{0K}|^2$. It is clear that the eigenstates are a coherent mixture at all Q except Q = 0. The latter follows from the fact that the exchange coupling must be zero at the origin. A detuning however imposes a momentum dependence on the eigenstates. Because the detuning counteracts the exchange coupling, the eigenstates must transform towards a pure K or K' state. In the limit of large Δ, the eigenstates are purely K or K' excitons. Also θ follows this pattern, as demonstrated in Figure 4.5.

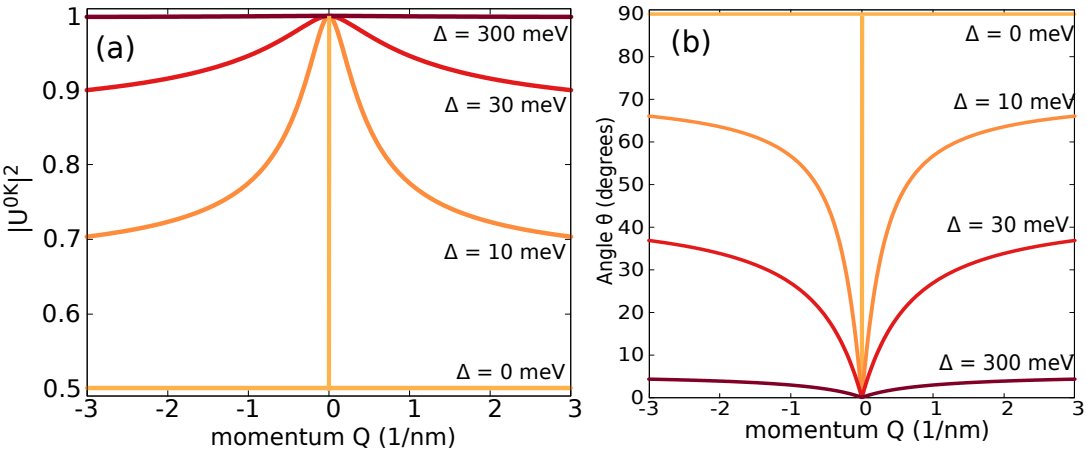

Figure 4.5: (a) Amount of K-likeness contributing to the eigenstates of the lower branch for a freestanding monolayer of MoSe2. (b) Azimuthal angle of the eigenstates in fucntion of momentum for different detunings.

5

Impact on the Exciton-Phonon Interaction

In this chapter the eigenstates from the exchange Hamiltonian are used to study the impact of the exchange coupling on exciton-phonon scattering. In order to do so, a transformation matrix is introduced that helps to perform a basis transform to the new eigenbasis $\{Y^{\dagger\sigma}_{\mathbf{Q}}, Y^{\sigma}_{\mathbf{Q}}\}$. In this way, a modified exciton-phonon coupling is obtained, which can be used to calculate the excitonic outscattering rates. These are discussed in the second part of this chapter.

5.1 Exciton-Phonon Coupling

In the previous chapter the eigenenergy and eigenstates were derived for the excitonic Hamiltonian with exchange coupling. These eigenstates can be used to write the excitonic operators $X^{\dagger\xi}_{\mathbf{Q}}, X^{\xi}_{\mathbf{Q}}$ in function of the transformed basis $\{Y^{\dagger\sigma}_{\mathbf{Q}}, Y^{\sigma}_{\mathbf{Q}}\}$. This is done by introducing a unitary matrix U, defined as

$$U^{\sigma K}_{\mathbf{Q}} = \frac{1}{\sqrt{1+|t^{\sigma}_{\mathbf{Q}}|^2}} \tag{5.1}$$

$$U^{\sigma K'}_{\mathbf{Q}} = \frac{t^{\sigma}_{\mathbf{Q}} e^{2i\theta}}{\sqrt{1+|t^{\sigma}_{\mathbf{Q}}|^2}} \tag{5.2}$$

Using $U^{\sigma\xi}_{\mathbf{Q}}$, with $\xi = K/K'$, one can express the excitonic operators as

$$X^{\xi}_{\mathbf{Q}} = \sum_{\sigma} U^{\sigma\xi}_{\mathbf{Q}} Y^{\sigma}_{\mathbf{Q}}. \tag{5.3}$$

By inserting equation 5.3 into the exciton-phonon Hamiltonian, one obtains the transformed exciton-phonon Hamiltonian

$$\hat{H}_{x-ph} = \sum_{\sigma\sigma'\alpha\mathbf{Q}\mathbf{q}} \mathcal{G}^{\sigma\sigma'\alpha}_{\mathbf{Q}\mathbf{q}} Y^{\dagger\sigma'}_{\mathbf{Q}+\mathbf{q}} Y^{\sigma}_{\mathbf{Q}} (b_{\mathbf{q}} + b^{\dagger}_{\mathbf{q}}). \tag{5.4}$$

where exchange exciton-phonon coupling is expressed by

$$\mathcal{G}^{\sigma\sigma'\alpha}_{\mathbf{Q}\mathbf{q}} = g^{\alpha}_{\mathbf{q}} \sum_{\xi} U^{\dagger\sigma'\xi}_{\mathbf{Q}+\mathbf{q}} U^{\sigma\xi}_{\mathbf{Q}}. \tag{5.5}$$

The exciton-phonon coupling element gives the probability for an exciton in band σ and momentum $\mathbf{Q}$ to scatter to band σ' with momentum $\mathbf{Q}+\mathbf{q}$. Interesting is the fact that the coupling element becomes dependent on the centre-of-mass momentum and the excitonic phase. The square of the exciton-phonon coupling can be expressed as $|\mathcal{G}^{\sigma\sigma'\alpha}_{\mathbf{Q},\mathbf{q}}|^2 = |g^{\alpha}_{\mathbf{q}}|^2 A^{\sigma\sigma'}_{\mathbf{Q},\mathbf{q}}(\theta)$, i.e. the coupling is modulated by a factor which depends explicitly on the phase. We will refer to this element as the 'modulation factor'. As an illustration, we consider the case $\Delta = 0$. The exciton-phonon coupling then simplifies to:

$$|\mathcal{G}^{\sigma\sigma'\alpha}_{\mathbf{Q},\mathbf{q}}|^2 = |g^{\alpha}_{\mathbf{q}}|^2 \frac{1+\tilde{\sigma}\cos(2\Delta\theta)}{2} \tag{5.6}$$

where $\tilde{\sigma} = -1$ if $\sigma \neq \sigma', \text{interbranch scattering}$ and $\tilde{\sigma} = +1$ if $\sigma = \sigma'$, intrabranch scattering. The argument of the cosine is defined as $\Delta\theta = \theta_{\mathbf{Q}+\mathbf{q}} - \theta_{\mathbf{Q}}$, i.e. the exciton-phonon coupling depends on the phase difference between initial and final state. Making a distinction between intrabranch scattering ($\tilde{\sigma} = -1$) and interbranch scattering ($\tilde{\sigma} = 1$), one finds that $A^{\sigma\sigma}_{\mathbf{Q},\mathbf{q}}(\theta) = \cos^2\Delta\theta$, $A^{\sigma\bar{\sigma}}_{\mathbf{Q},\mathbf{q}}(\theta) = \sin^2\Delta\theta$, respectively.

The phase-dependence is visualised in Figure 5.1. More specifically, the figure shows the acoustic part of the exciton-phonon coupling, normalised to the highest value. The exciton-phonon coupling is a measure for the probability of an exciton scattering out of state (Q_x, Q_y) with a phonon of momentum q. It is clear that at small centre-of-mass momentum, the exciton-phonon coupling exhibits a strong phase-selectivity which depends on the phonon momentum as well. Figure 5.1 shows the coupling element for three different values of the phonon momentum q. It is clear that the larger the phonon momentum, the further the phase-selectivity extends in exciton momentum space.

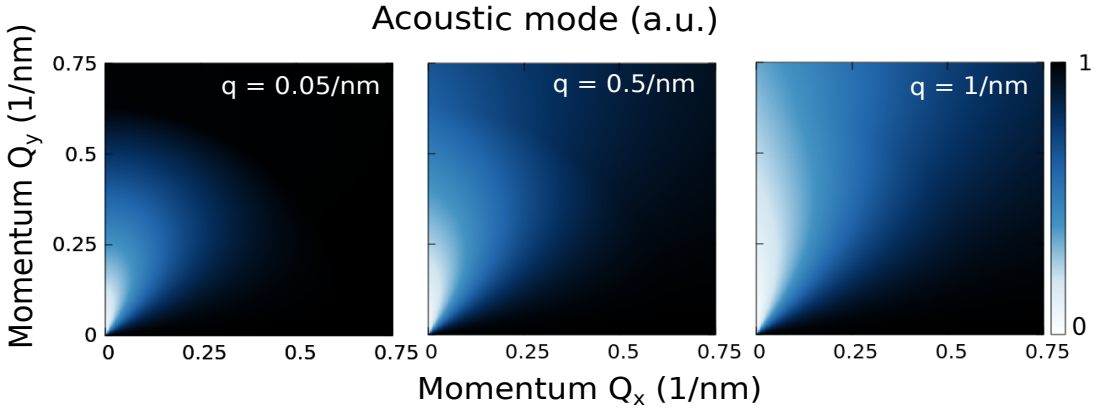

Figure 5.1: Normalised acoustic mode of $|G^{\sigma\sigma}_{\mathbf{Q},\mathbf{q}}|^2$, for three different phonon momenta. A relative dielectric constant of 1 was used. It is clear that the coupling element depends on the excitonic phase and momentum. The

Scattering changes when a magnetic field is imposed. Figure 5.2 shows the modulation factor $A^{\sigma\sigma}_{\mathbf{Q},\mathbf{q}}(\theta)$ for 3 different values of the detuning. From the earlier discussion, we know that at $\Delta = 0$, the modulation factor is a $\cos^2\Delta\theta$. With magnetic field, the modulation factor changes, i.e. the phase-selectivity is no more centred at the origin

and decreases with magnetic field. To see this better, one can compare the colour scales between the subfigures in Figure 5.2. The with increasing magnetic field, the colours become darker, i.e. the lower bound of the modulation factor moves to 1. At $\Delta = 50$ meV, the modulation factor the lower bound of the modulation factor will already have increased to 0.75. This indicates that the coupling goes back to $|g^{\alpha}_{\mathbf{q}}|$. This is a direct consequence of the decoupling of the K and K' valley by means of a magnetic field.

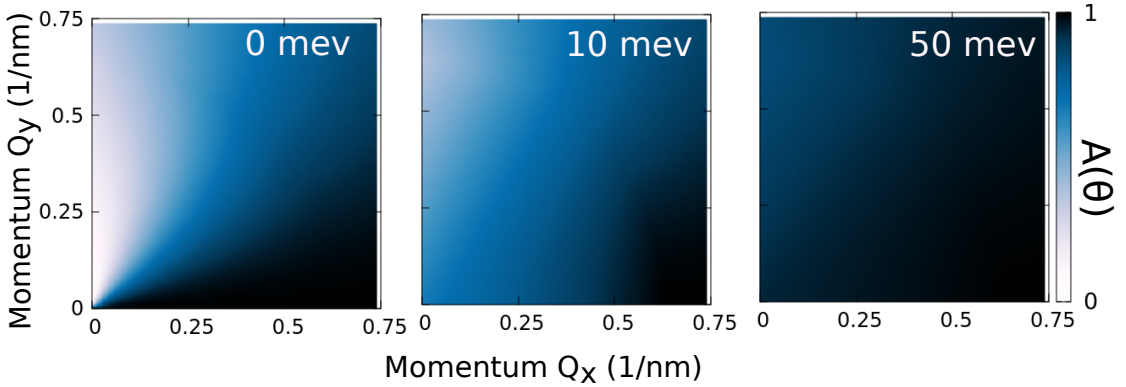

Figure 5.2: Modulation factor $A^{\sigma\sigma}_{\mathbf{Q},\mathbf{q}}(\theta)$ with q=1/nm for a freestanding monolayer $\Delta = 0, 10, 50$ meV. From the colour scale one can see that the coupling element shifts to 1 with increasing magnetic field.

5.2 Scattering Rates

Due to the transformed band structure and exciton-phonon coupling, one can expect that the exciton-phonon dynamics changes. In order to study the influence of the exchange coupling on the exciton dynamics, we introduce the phonon-assisted excitonic scattering rates [9]. The excitonic scattering rates can be derived from the semiconductor Bloch equations, using a Born-Markov approximation [10]. The result is an equation that resembles Fermi's golden rule:

$$\Gamma^{\sigma}_{\mathbf{Q}} = \frac{2\pi}{\hbar} \sum_{\sigma' \pm \alpha \mathbf{q}} |\mathcal{G}^{\sigma\sigma'\alpha}_{\mathbf{Q},\mathbf{q}}|^2 (\frac{1}{2} \pm \frac{1}{2} + n^{\alpha}_{\mathbf{q}}) \delta(\tilde{E}^{\sigma'}_{\mathbf{Q}+\mathbf{q}} - \tilde{E}^{\sigma}_{\mathbf{Q}} \pm \hbar\omega^{\alpha}_{\mathbf{Q}}), \tag{5.7}$$

with $n^{\alpha}_{\mathbf{q}}$ the phonon occupation number, defined by the Bose distribution. The sum over $\pm$ expresses the emission (+) and absorption (-) of phonons. Note that the emission contains $(1+ n^{\alpha}_{\mathbf{q}})$, where the 1 stands for spontaneous phonon emission and $n^{\alpha}_{\mathbf{q}}$ for stimulated phonon emission. The δ-function in the end accounts for the conservation of energy.

5.2.1 Numerical Treatment

A standard procedure for treating equation 5.7 numerically is to transform the sum to an integral and rewrite the δ-function as:

$$\delta(f(Q)) = \sum_i \frac{\delta(Q - Q_i)}{df/dQ}\bigg|_{Q_i} \tag{5.8}$$

where Q_i denotes the zeros of the argument f(Q). However, this rule can only be used as long as the derivative of the argument is nonzero for all Q_0. This poses problems on the treatment of the scattering rate as the derivative of the argument can vanish in the acoustic terms.

An alternative way to treat the problem is to assume a constant broadening of the energy conservation, i.e. the δ-function is replaced by a Lorentzian with broadening γ. In fact, this treatment lies closer to experiment, as in reality a broadening will occur. The equation for the scattering rate then becomes

$$\Gamma^{\sigma}_{\mathbf{Q}} = \frac{2\pi}{\hbar} \sum_{\sigma' \pm \alpha} \frac{A}{4\pi^2} \int dq d\theta |\mathcal{G}^{\sigma\sigma'\alpha}_{\mathbf{Q},\mathbf{q}}|^2 (\frac{1}{2} \pm \frac{1}{2} + n^{\alpha}_{\mathbf{q}}) \mathcal{L}_{\gamma}(\tilde{E}^{\sigma'}_{\mathbf{Q}+\mathbf{q}} - \tilde{E}^{\sigma}_{\mathbf{Q}} \pm \hbar\omega^{\alpha}_{\mathbf{Q}}). \tag{5.9}$$

with A the sheet area. As a reasonable and numerically less intensive value for the broadening, we take $\gamma = 1$ meV. In order to numerically implement the equation, the integral can be expressed as a Riemann sum so that the equation becomes:

$$\Gamma^{\sigma}_{\mathbf{Q}} = \frac{2\pi}{\hbar} \sum_{\sigma' \pm \alpha} \sum_{\Delta q \Delta\theta} \frac{\Delta q \Delta\theta}{4\pi^2} |\mathcal{G}^{\sigma\sigma'\alpha}_{\mathbf{Q},\mathbf{q}}|^2 (\frac{1}{2} \pm \frac{1}{2} + n^{\alpha}_{\mathbf{q}}) \mathcal{L}_{\gamma}(\tilde{E}^{\sigma'}_{\mathbf{Q}+\mathbf{q}} - \tilde{E}^{\sigma}_{\mathbf{Q}} \pm \hbar\omega^{\alpha}_{\mathbf{Q}}). \tag{5.10}$$

5.2.2 Discussion

In order to understand the impact of the scattering rate on the scattering rate, it is good to shortly look at the result of the scattering rate without exchange coupling, shown in Figure 5.3. The scattering rate has two main regions: at small momentum, scattering is dominated by acoustic absorption of phonons. At larger momentum, excitons reach the point at which their energy equals the optical phonon energy. This means that they can emit phonons to the bottom of the band, resulting in a large increase in scattering due to optical phonon emission.

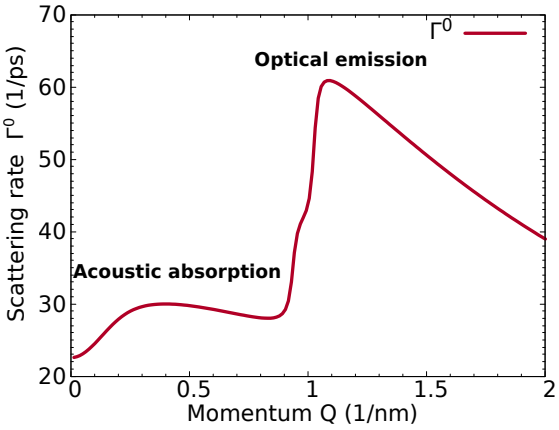

Figure 5.3: Scattering rate of the parabolic band structure.

The results for the case with exchange coupling are shown in Figure 5.4a. More specifically it shows the scattering rates for the lower branch (LB) and upper branch (UB). The dashed line denotes the case where the valleys are uncoupled, which we will refer to as Γ^0. By looking at equation 5.7, we see that two factors differ from the uncoupled case: the modified band structure in the Lorentzian, which will account for new scattering channels, and the modified exchange-phonon coupling. There are three regions in momentum space that differ significantly from Γ^0, denoted with A, B and C. Figure 5.4b visualises the scattering channels in the band structure.

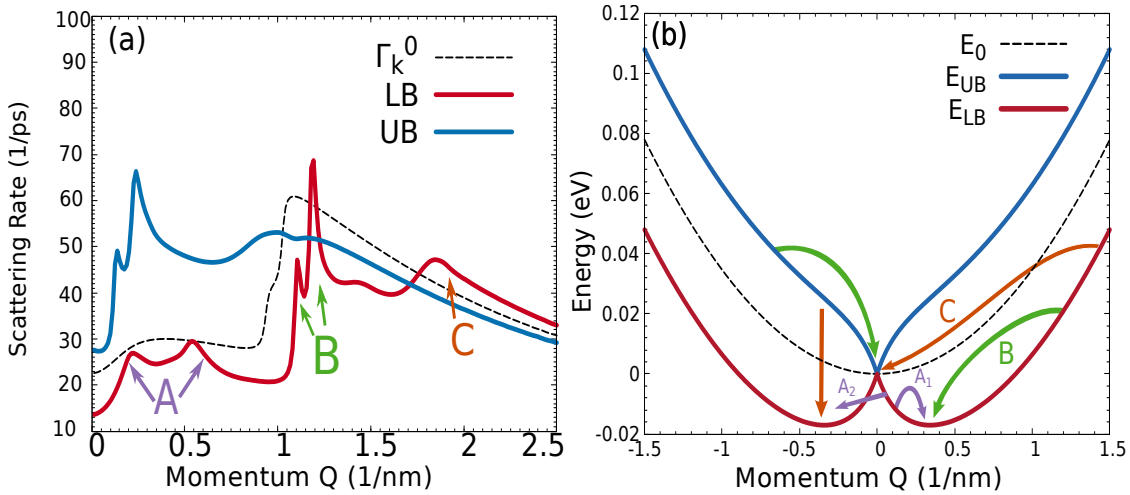

Figure 5.4: (a)Scattering rate of the modified band structure at 300 K. The red line denotes the scattering rate of the lower branch, blue the scattering rate of the lower branch and the dashed line the scattering rate of the uncoupled case. (b) the origin of the peaks in the scattering rate can be found in the band structure. The arrows denote possible types of scattering channels which are also rotational symmetric. A1,A2,B and C are the scattering channels that belong to the peaks indicated in (a).

Region A consists of 2 hills arising from scattering with acoustic phonons. In contrast to Γ^0, both absorption and emission of phonons are important here, as Figure 5.5

shows. Obviously, at the band minima, no phonons can be emitted, so there only absorption occurs. From considering conservation of energy, two different types of acoustic emission channels can be recognised. A1 denotes the emission of an acoustic phonon from the lower branch to the band minimum in the same 'valley' of the lower branch. Besides, energy conservation allows excitons at one side of the lower branch to emit acoustic phonons to the opposite band minimum, denoted by A2. However, note that due to the Lorentzian broadening, the maxima of the emission peaks are shifted.

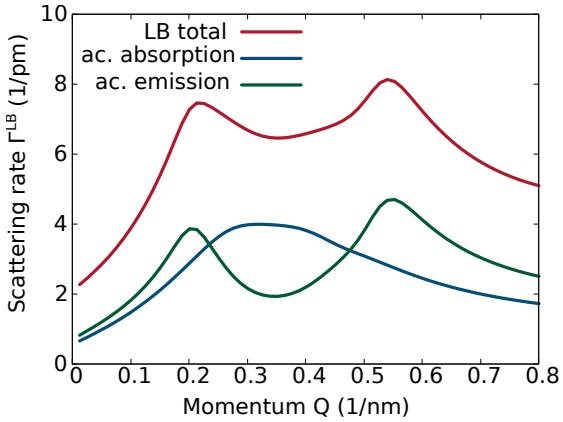

Figure 5.5: Total LB scattering rate in the low momentum regime at 100 K. The shape of the scattering rate is determined by the acoustic phonon emission and absorption.

At higher momenta, the optical phonons start to play a role, analogous to Γ^0. Remember that the optical dispersion is constant and that there are three optical modes from which the two largest are approximately equal, see appendix B. Because of the shift in the exchange band structure, the point at which the optical phonon energies are reached, occurs is different for the LB and UB. This explains the shift in the optical emission peaks in the modified scattering rates compared to Γ^0. Note that the LB emission peaks come from optical intrabranch emission whereas the UB emission peaks come from optical interbranch emission. Finally, channel C denotes the elevation in the tail of the scattering rate. For the lower branch, the scattering comes from the optical emission of phonons to the upper branch, whereas the elevation in the UB scattering rate is due to the intrabranch emission of optical phonons to the bottom of the upper branch.

5.2.3 Influence of the phase and magnetic field dependence

An important fact that we have not discussed so far is the fact that the LB scattering rates lie below Γ^0. By only considering conservation of energy, one would expect an increased scattering rate because of the extra scattering channels. However, this is not the case. The answer to this paradox is to find in the exciton-phonon coupling. Figure 5.6a shows the acoustic region of the scattering rate, calculated with and without the phase-dependence ($\Delta\theta = 0$).

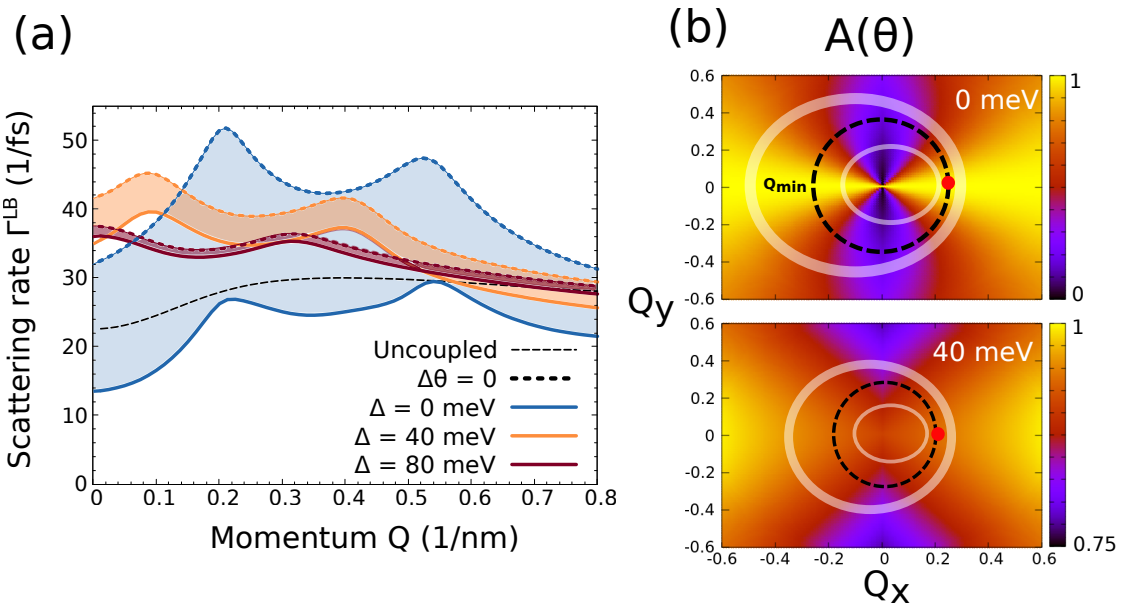

Figure 5.6: (a) Acoustic part of the LB scattering rate for a freestanding monolayer, 300 K: comparison between scattering rate with and without phase-dependence. (b) Modulation factor for intraband scattering at $\Delta = 0, 40$ meV. The ellipses denote the crossection of the acoustic dispersion cone, starting at the point of the band minimum denoted by the red dot. The dashed line denotes the global band minimum of the band structure.

It is clear that without the phase-dependence, the scattering rate would be highly increased. The reason for the decrease is the fact that the modulation factor $A^{\sigma\sigma}(\theta) = \cos^2 \Delta\theta$ at zero detuning, removes a significant part of the available scattering states. The upper part of Figure 5.6b shows the modulation factor at zero detuning. The dashed circle is a sketch of the band minimum and the white ellipses denote scattering crossection of the lower branch with the conical acoustic dispersion, starting at the band minimum indicated by a red dot. From this figure it is clear that the modulation factor takes out a significant part of the available scattering states. Next, when a magnetic field is imposed, we know from section 4 that the band structure narrows down and the eigenstates move towards pure K or K' states. Also the exciton-phonon coupling has a similar behaviour as was shown in the beginning of this chapter. Figure 5.7 shows the behaviour of the acoustic part of the scattering rate in function of detuning and centre-of-mass momentum. Interestingly, the scattering rate knows an upward trend up to 45 meV, after which

it decreases, denoted by the blue and green arrows respectively in Figure 5.7a. This is a non-trivial result.

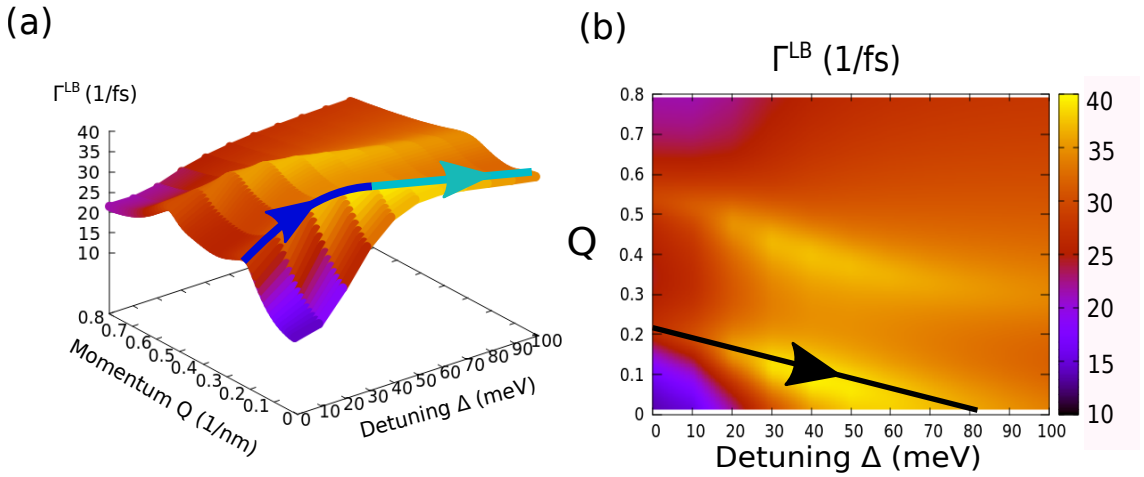

Figure 5.7: Acoustic part of the LB scattering rate for a freestanding monolayer, 300 K: (a)surface plot, arrows stress the increasing and decreasing parts in function of detuning.(b) Heat map showing the scattering rate in a. Arrow denotes the shift in the emission peaks due to the changing band structure.

In order to explain this behaviour we go back to Figure 5.6a. A key here is the fact that the scattering rate without phase-dependence continuously decreases with magnetic field. Further, the difference between the phase-dependent and -independent rates becomes smaller with magnetic field. The former must be explained by the scattering crossection. Because the band structure narrows down, the number of available scattering states decreases, as Figure 5.6b shows for 0 and 40 meV. The latter implies is explained by the fact that the phase-dependence of the exciton-phonon matrix element becomes weaker. As Figure 5.6b shows, the lower bound of the modulation factor increases to 0.75. Also the shape of the modulation factor blurs out, so that larger regions of the scattering crossection can contribute more significantly. Therefore we can conclude that there is a competition between the number of states and the modulation factor. At small detuning, the increase of states due to the weakening of the modulation factor is larger than the decrease of excitonic states due to the narrowing of the branch. This results in an increase of the scattering rate. Then, when the modulation factor starts saturating, the decrease in the number of states takes over, hence the scattering rate decreases until it saturates.
The last influence of the narrowing band structure is shown in Figure 5.7b. This Figure shows the heat map of the scattering rate in function of momentum and detuning. The black arrow indicates how the hills of the scattering rate move towards the origin. Due to the narrowing band structure, the band minimum shifts to smaller momenta until it coincides with the centre of the band structure. A similar thing happens with the points from which emission of acoustic phonons can occur. Because the hills of acoustic phonon emission relate directly to the band structure, the hills shift towards smaller momenta until they disappear and the uncouled scattering rate is retrieved.

5.2.4 Influence of Encapsulation and Temperature dependence

From Figures 5.8 and 5.9, we see that the scattering rate in an encapsulated monolayer is slightly different compared to the uncoupled case. Figure 5.8 shows the scattering rates for (a) a freestanding monolayer of MoSe2 and (b) a monolayer with hBN encapsulation, at different temperatures. The first thing that draws attention is the fact that the increase at large momentum due to interbranch scattering (see scattering channel C) occurs at lower momentum than the freestanding monolayer. This is due to the fact that that the band structure is shallower than the freestanding monolayer, which means that optical emission and interbranch emission occur at lower momentum. Another interesting and important feature is the fact that the acoustic hills lie above Γ^0. The argument for this increase is similar to the argument for the magnetic field dependence. At zero magnetic field, the exciton-phonon coupling is comparable to coupling of the freestanding monolayer. The band structure however can be compared to the one of the freestanding monolayer with a small detuning imposed. For this reason, fewer states lie in the region where the modulation factor is minimum and by consequence the scattering is larger. Lastly, comparing the temperature dependence for both cases, we observe a similar trend in function of temperature. At low temperatures, the difference between the scattering rate and Γ^0 is small. However, when temperature increases, the difference becomes more pronounced. An important thing to note is that the difference in scattering rate at Q=0 with Γ^0 increases, with the scattering rates going down with temperature.

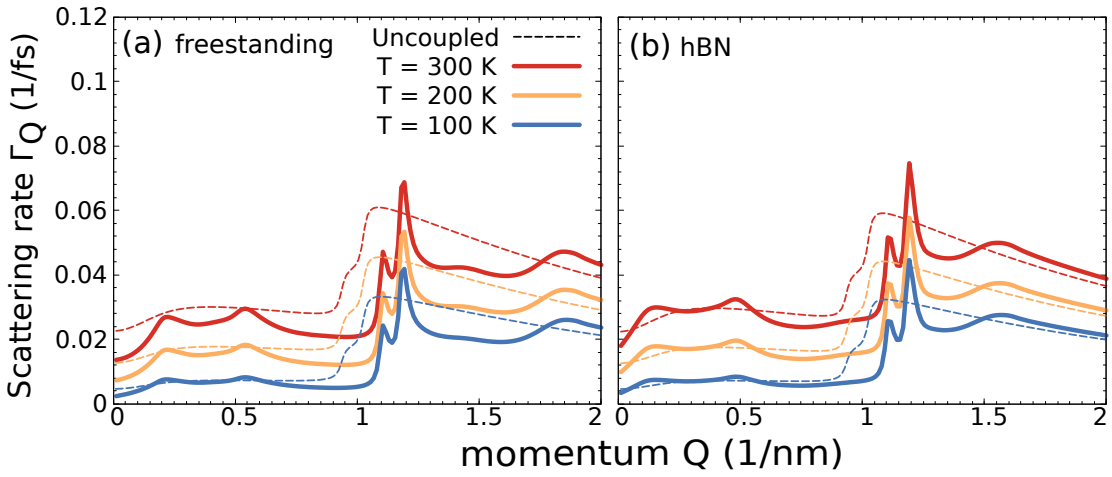

Figure 5.8: Influence of the temperature on the scattering rate of the lower branch for (a) freestanding monolayer, (b) hBN encapsulation.

The magnetic field dependence of the freestanding monolayer and the encapsulated monolayer is shown in Figure 5.9a and 5.9b. The behaviour of both monolayers is explained as discussed in section 5.2.3. The important difference is the fact that the valleys of the encapsulated monolayer decouple much faster with detuning, which means that also the scattering rate moves back faster. Hence, the saturation of the scattering rate occurs at significantly lower detuning than the freestanding monolayer.

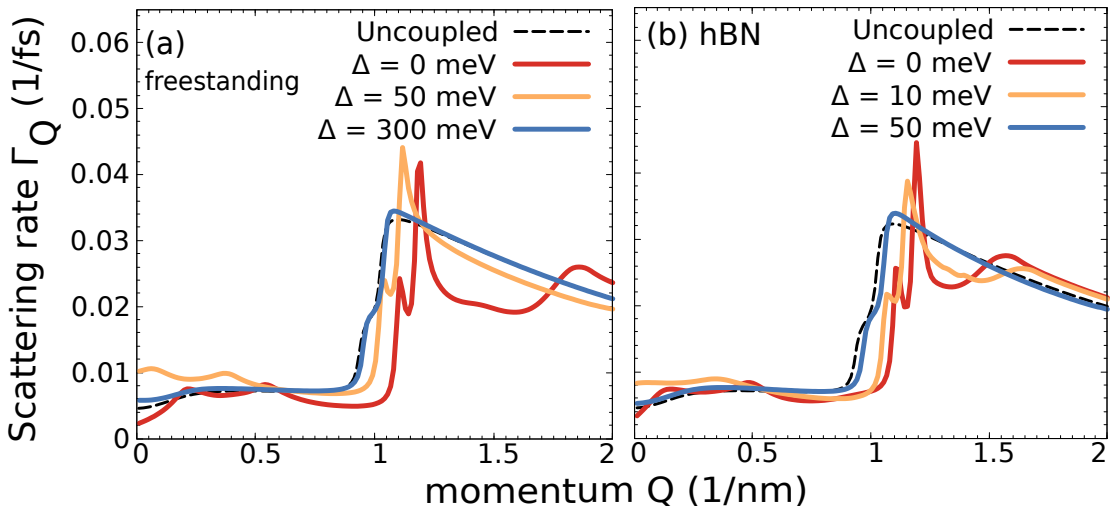

Figure 5.9: Influence of detuning on the scattering rate of the lower branch for (a) freestanding monolayer, (b) hBN encapsulation.

6

Diffusion Coefficient

Finally, we can use our knowledge about exciton-phonon scattering and apply it to a measurable quantity, the diffusion coefficient. The diffusion coefficient can be derived by calculating the equation of motion for the Wigner function. This is described in the first section. The second section discusses the results of the diffusion coefficients.

6.1 Wigner function and equation of motion

The diffusion coefficient can be microscopically derived by introducing the Wigner function for excitons with exchange interaction:

$$N^{\sigma}_{\mathbf{Q}} = \sum_{\mathbf{q}} N^{\sigma}_{\mathbf{Q}-\frac{1}{2}\mathbf{q},\mathbf{Q}+\frac{1}{2}\mathbf{q}} e^{i\mathbf{q}\cdot\mathbf{r}} \tag{6.1}$$

where $N^{\sigma}_{Q,Q'} = \left\langle Y^{\dagger\sigma}_{Q} Y^{\sigma}_{Q'} \right\rangle$, which can be seen as an off-diagonal density matrix. The Wigner function was introduced by Eugene Wigner in 1932 to study the influence of quantum mechanics on statistical mechanics theory [18]. Because of the uncertainty principle of quantum mechanics, the Wigner function can assume negative values, in contrast to classical distribution functions, it is classified as a quasi-probability distribution. More on the Wigner function can be found in [19]. By integrating the Wigner function over momentum, the spatial distribution is obtained (and vice versa):

$$N(\mathbf{r}) = \sum_{\mathbf{Q}\sigma} N^{\sigma}_{\mathbf{Q}} \tag{6.2}$$

An equation of motion for the Wigner function can be found by applying the Heisenberg equation of motion with the transformed exciton Hamiltonian to the off-diagonal density matrix $N^{\sigma}_{\mathbf{Q},\mathbf{Q}'}$, which results in

$$i\hbar\partial_t N^{\sigma} = (E^{\sigma}_{\mathbf{Q}} - E^{\sigma}_{\mathbf{Q}'}) N^{\sigma}_{\mathbf{Q}\mathbf{Q}'} \tag{6.3}$$

In order to obtain the Wigner function, we transform the coordinates as
$\mathbf{Q} \to \mathbf{Q} - \frac{1}{2}\mathbf{q}$, $\mathbf{Q}' \to \mathbf{Q} + \frac{1}{2}\mathbf{q}$.
Further, by taking the Fourier transform over $\mathbf{q}$, one arrives at:

$$i\hbar\partial_t N^\sigma_{\mathbf{Q}} = \sum_{\mathbf{q}} (E^\sigma_{\mathbf{Q}+\frac{1}{2}\mathbf{q}} - E^\sigma_{\mathbf{Q}+\frac{1}{2}\mathbf{q}}) N^\sigma_{\mathbf{Q}-\frac{1}{2}\mathbf{q},\mathbf{Q}+\frac{1}{2}\mathbf{q}} e^{i\mathbf{q}\cdot\mathbf{r}} \tag{6.4}$$

$$= \nabla_{\mathbf{Q}} E^\sigma_{\mathbf{Q}} \sum_{\mathbf{q}} \mathbf{q} N^\sigma_{\mathbf{Q}-\frac{1}{2}\mathbf{q},\mathbf{Q}+\frac{1}{2}\mathbf{q}} e^{i\mathbf{q}\cdot\mathbf{r}} \tag{6.5}$$

In the second step, the definition of the derivative was used to write the energy difference as a gradient. By using the quantum mechanical expression for momentum, $\mathbf{q} = \frac{1}{i}\nabla_{\mathbf{r}}$, the equation of motion for the Wigner function is found

$$\partial_t N^\sigma_{\mathbf{Q}} = -v^\sigma_{\mathbf{Q}} \cdot \nabla_{\mathbf{r}} N^\sigma_{\mathbf{Q}}(\mathbf{r}) \tag{6.6}$$

where $v^\sigma_{\mathbf{Q}} = \frac{1}{\hbar}\nabla_{\mathbf{Q}} E^\sigma_{\mathbf{Q}}$ is the group velocity. The next part of the derivation is a standard procedure that includes the Boltzmann scattering term in the equation of motion.

6.1.1 Boltzmann Scattering

To proceed with the derivation of the diffusion coefficient, exciton-phonon scattering has to be included in the equation of motion. In a semi-classical picture, this is done by including the Boltzmann scattering integral in the equation of motion [20, 21, 22]. Assuming small deviations from equilibrium, the Wigner function can be written as

$$N^\sigma_{\mathbf{Q}}(\mathbf{r}) = N^{(0)\sigma}_{\mathbf{Q}}(\mathbf{r}) + \delta N^\sigma_{\mathbf{Q}}(\mathbf{r}), \tag{6.7}$$

where $N^{(0)\sigma}_{\mathbf{Q}}(\mathbf{r}) = N^0(\mathbf{r},t)e^{-E^\sigma_{\mathbf{Q}}/k_B T}$ is the near-equilibrium distribution and $\delta N^\sigma_{\mathbf{Q}}(\mathbf{r})$ the deviation from equilibrium. Further, k_B denotes the Boltzmann constant and T the temperature. An important property needed later is the conservation of carriers, which means that $\sum_{\mathbf{Q}} \delta N^\sigma_{\mathbf{Q}}(\mathbf{r}) = 0$. In relaxation time approximation, the Boltzmann collision term contributes to the equation of motion with $\delta N^\sigma_{\mathbf{Q}}$:

$$\partial_t N^\sigma_{\mathbf{Q}} - v^\sigma_{\mathbf{Q}} \cdot \nabla_{\mathbf{r}} N^\sigma_{\mathbf{Q}} = -\frac{\delta N^\sigma_{\mathbf{Q}}}{\tau^\sigma_{\mathbf{Q}}} \tag{6.8}$$

Inserting equation 6.7 in this expression and noting that , $\partial_t \delta N^\sigma_{\mathbf{Q}}$ can be neglected as the departure of equilibrium is small, one arrives at a Boltzmann equation for the exciton-phonon scattering:

$$\delta N^\sigma_{\mathbf{Q}} = -\tau^\sigma_{\mathbf{Q}}(v^\sigma_{\mathbf{Q}} \cdot N^\sigma_{\mathbf{Q}}(\mathbf{r}) + \partial_t N^{(0)\sigma}_{\mathbf{Q}}) \tag{6.9}$$

6.1.2 Diffusion Coefficient

Then, using the Boltzmann equation, conservation of particle number and equation 6.2, we can find an equation of motion for the the spatial distribution function

$$\partial_t N(\mathbf{r}) \approx \sum_{\mathbf{Q}\sigma} v^\sigma_{\mathbf{Q}} \cdot \nabla_{\mathbf{r}} [v^\sigma_{\mathbf{Q}} \cdot \nabla_{\mathbf{r}} N^{(0)\sigma}_{\mathbf{Q}}] \tag{6.10}$$

where we used that $\Gamma^\sigma_{\mathbf{Q}} \delta N^\sigma_{\mathbf{Q}}$ is small, as well as the spatial and time derivatives of the near-equilibrium distribution. A last important derivation from equation 6.2 gives an expression for the spatial distribution function:

$$N^{(0)\sigma}_{\mathbf{Q}} = N(\mathbf{r}) \frac{e^{E^\sigma_{\mathbf{Q}}/k_B T}}{\mathcal{Z}} \tag{6.11}$$

with $\mathcal{Z} = \sum_{\mathbf{Q}\sigma} e^{E^\sigma_Q}$ the partition sum. Equation 6.10 becomes:

$$\partial_t N(\mathbf{r}) = \sum_{\mathbf{Q}\sigma} v^\sigma_{\mathbf{Q}} \cdot \nabla_{\mathbf{r}} [v^\sigma_{\mathbf{Q}} \cdot \nabla_{\mathbf{r}} N(\mathbf{r}) \frac{e^{E^\sigma_{\mathbf{Q}}/k_B T}}{\mathcal{Z}}] \tag{6.12}$$

Writing out the equation into vector components, and noting that the spatial derivative of the group velocity is zero, one arrives at

$$\partial_t N(\mathbf{r}) = \sum_{i,j} \partial^2_{ij} N(\mathbf{r}) \sum_{\mathbf{Q},\sigma} \frac{(v^\sigma_{\mathbf{Q}})_i (v^\sigma_{\mathbf{Q}})_j}{\Gamma^\sigma_{\mathbf{Q}}} \tag{6.13}$$

where the indices i,j denote the vector components in two dimensions. Because the group velocity is an uneven function, the sum over the off-diagonal contributions vanishes. Finally, one arrives at Fick's second law of diffusion, which reads:

$$\partial_t N(\mathbf{r}) = D \Delta N(\mathbf{r}) \tag{6.14}$$

where the diffusion coefficient is defined as

$$D = \frac{1}{2} \sum_{\mathbf{Q}\sigma} \frac{|v^\sigma_{\mathbf{Q}}|^2}{\Gamma^\sigma_{\mathbf{Q}}} \frac{e^{-E^\sigma_{\mathbf{Q}}/k_B T}}{\mathcal{Z}} \tag{6.15}$$

with $v^\sigma_{\mathbf{Q}}$ the group velocity, $\Gamma^\sigma_{\mathbf{Q}}$ the scattering rate and $\frac{e^{-E^\sigma_{\mathbf{Q}}/k_B T}}{\mathcal{Z}}$ the exciton Boltzmann distribution with k_B the Boltzmann constant, T the temperature and $\mathcal{Z} = \sum_{\mathbf{Q}\sigma} e^{-E^\sigma_{\mathbf{Q}}/k_B T}$ the partition sum.

6.2 Results

Equation 6.15 gives the key to predict the impact of the exchange coupling on the diffusion coefficient from microscopic quantities, i.e. the scattering rates, the group velocity and the occupation number. Figure 6.1 shows the resulting diffusion coefficient in function of detuning for a freestanding monolayer of MoSe2. The dashed lines denote the diffusion coefficient without exchange coupling, referred to as D^0. Note that the equation for D^0 is the same as equation 6.15, with the difference that there is just one branch in the band structure. Also, note that D^0 is independent of detuning. Indeed, both Γ^0 as well as the group velocity don't depend on detuning, D^0 must be constant in detuning.
In contrast, because of the changes in band structure and scattering rates due to the exchange coupling, the diffusion coefficient with inclusion of the exchange coupling varies with magnetic field. Furthermore, because the scattering rate increases with temperature, the diffusion coefficient is expected to decrease with temperature in both the coupled and uncoupled case.

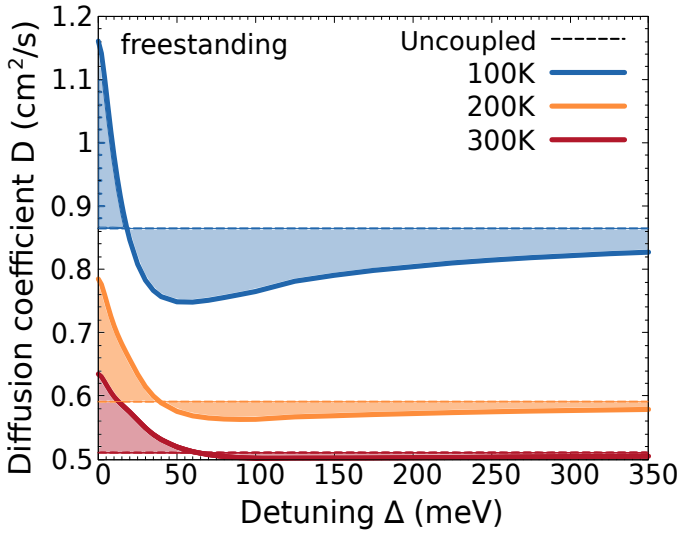

Figure 6.1: Diffusion coefficient in function of detuning for a freestanding monolayer of MoSe2.

6.2.1 Magnetic field dependence

A first thing to note in the expression of the diffusion coefficient for the coupled case, is the change in group velocity, shown in Figure 6.2a, compared to the uncoupled case. Where the latter is zero at Q=0, the former is zero at the band minima of the lower branch. Also, the group velocity of the modified case is highly increased at Q=0. This means that the exchange coupling results in fast excitons in the centre of the exchange band structure. When a magnetic field is imposed, the local maximum of the lower branch starts smoothing out, by which the group velocity becomes zero at the centre, though it is still large in the region around it. Also, note that the excitons have no velocity at the band minima. The important contribution from the scattering rate will be the tail at Q=0, which varies strongly with magnetic field as Figure 6.2b shows. Because the diffusion coefficient is divided by the scattering rate, it is useful to refer to its inverse, called the lifetime. As the scattering rate is minimal at the centre, this mean that the excitons at the centre of the band structure not only have a large group velocity, but also a large lifetime.

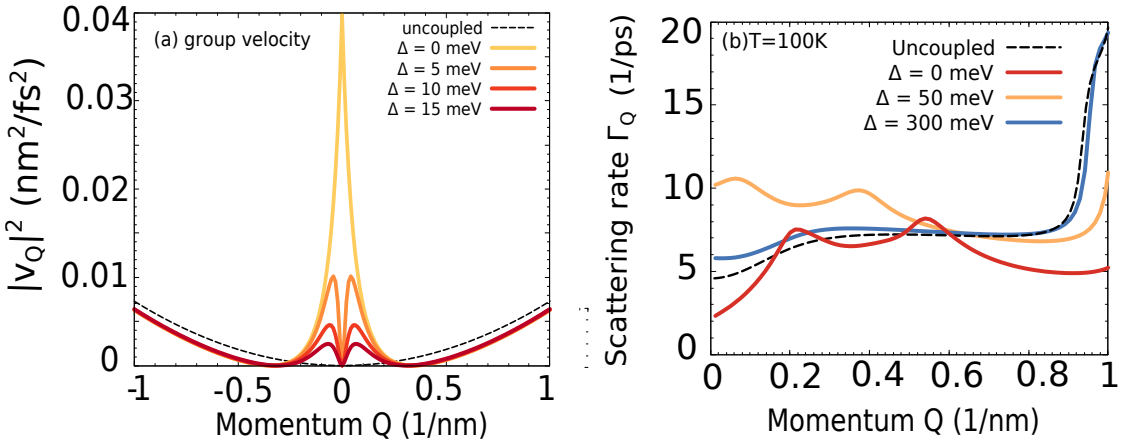

Figure 6.2: (a) group velocity in for different magnetic fields. (b) scattering rate for a freestanding monolayer at 100 K.

The last factor in the diffusion coefficient is the Boltzmann distribution, shown in Figure 6.3. The Boltzmann distribution gives a weight to every part of momentum space in accordance to the energy of that state. It is centered at the band minimum and decays to zero at larger momenta. Note that the distribution is smaller at Q=0 due to the local maximum in energy, but it is not negligible. For this reason, the increased group velocity will be able to play an important role. Note further that the Boltzmann distribution increases with magnetic field until it reaches a maximum at Q=0, equal to the uncoupled case. Note also that, because of the splitting of the band structure, the Boltzmann distribution of the upper branch is negligible, which allows us to leave it out of discussion.

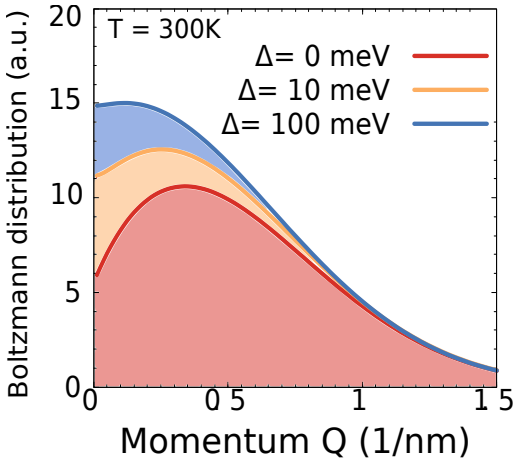

Figure 6.3: Boltzmann distribution for the lower branch for different magnetic fields at 300K.

Now we can start with analysing the behaviour of the diffusion coefficient in function of magnetic field. The curve can be split into three regions indicated by Figures 6.4a-c. This figure shows the momentum-resolved diffusion coefficients over which one integrates to obtain the final diffusion coefficient. The dashed line denotes $D^0(Q)$ and is constant in magnetic field. Figure 6.4a shows an example of the first regime in which the diffusion coefficient is maximal. It is clear that the increase comes from the part at small momentum, which arises from the product of the exciton lifetime and the group velocity. Because the excitons have large group velocity and lifetime when $\Delta = 0$, their diffusion is enhanced. When a small detuning is imposed, the group velocity decreases and the scattering rate increases. Hence the diffusion coefficient starts decreasing. The decreasing trend of the diffusion coefficient continues as detuning increases. Figure 6.4b shows that the increased part rapidly reduces for a detuning between 25-50 meV. This is the point at which the group velocity become negligible at small momenta and the lifetime is minimal, i.e. the scattering rate reaches its turning point. From then on the lifetime starts increasing and the diffusion coefficient grows until it reaches D^0, which Figure 6.4c indicates.

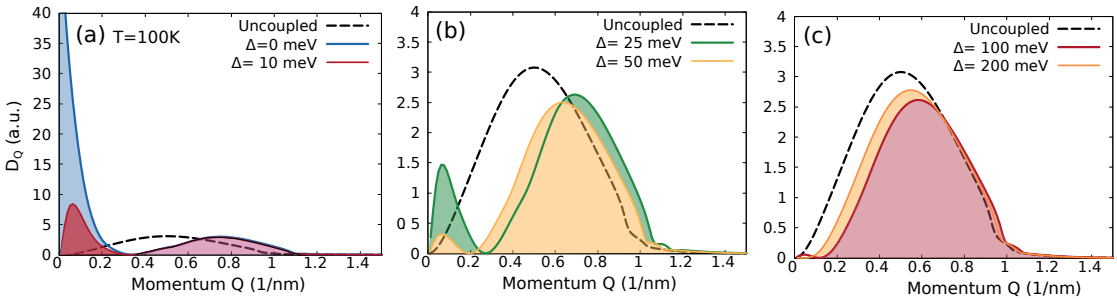

Figure 6.4: Momentum resolved diffusion coefficients for a freestanding monolayer at 100K. Three regions in detuning can be separated (a) small detuning at which the group velocity and lifetime are increased, (b) the transition where the group velocity and lifetime become smaller than the uncoupled case , (c) the regime in which the diffusion coefficient moves back to D^0.

6.2.2 Temperature dependence

Figure 6.5a shows the Boltzmann distribution at different temperatures. It is clear that the distribution gives more weight to states at low energy when the temperature is small. When temperature increases, the tail of the distribution extends to larger momenta, hence selecting a broader window. Figure 6.5b shows the scattering rates at different temperatures. The scattering rates at Q=0 increase with temperature, which means that the lifetime decreases. Hence, the increase in diffusion coefficient at zero detuning becomes less pronounced. Further, the difference between the minimum of the diffusion coefficient with exchange coupling and D^0 seems to decrease with temperature, resulting in a faster saturation at higher temperatures. This is explained by the fact that the Boltzmann distribution at larger temperatures is flatter and extends to larger momenta. Hence the influence of the acoustic part of the scattering rate is diminished. Now also, the optical part of the scattering rate plays a role. This part only has a monotonous increase towards Γ^0, which means that the diffusion coefficient in general saturates faster at larger temperatures.

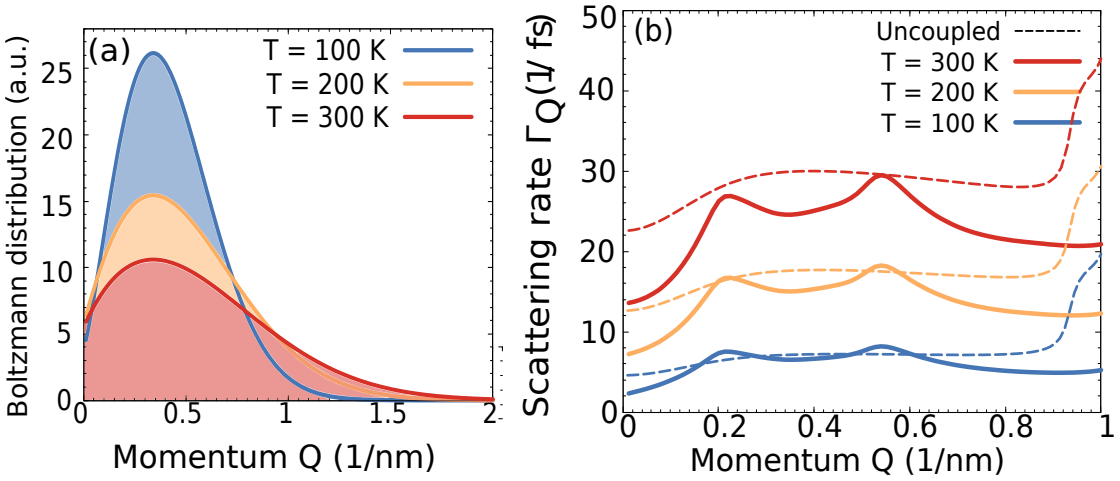

Figure 6.5: (a) Boltzmann distribution at different temperatures. (b) scattering rates at different temperatures.

6.2.3 Influence of encapsulation

The diffusion coefficient in function of detuning for an encapsulated monolayer is shown in Figure 6.6. In contrast to the freestanding monolayer, the encapsulated monolayer does not have a large increase; Instead, it starts about the value of D^0. The explanation is though similar to the freestanding monolayer. Because the scattering rates already start at a level larger than or comparable to Γ^0, there is an immediate decrease in the diffusion coefficient. Besides, the increase in group velocity is negligible compared to the uncoupled case. Lastly, the scattering rates also saturate much quicker with magnetic field, which results in the diffusion coefficient saturating quickly with detuning.

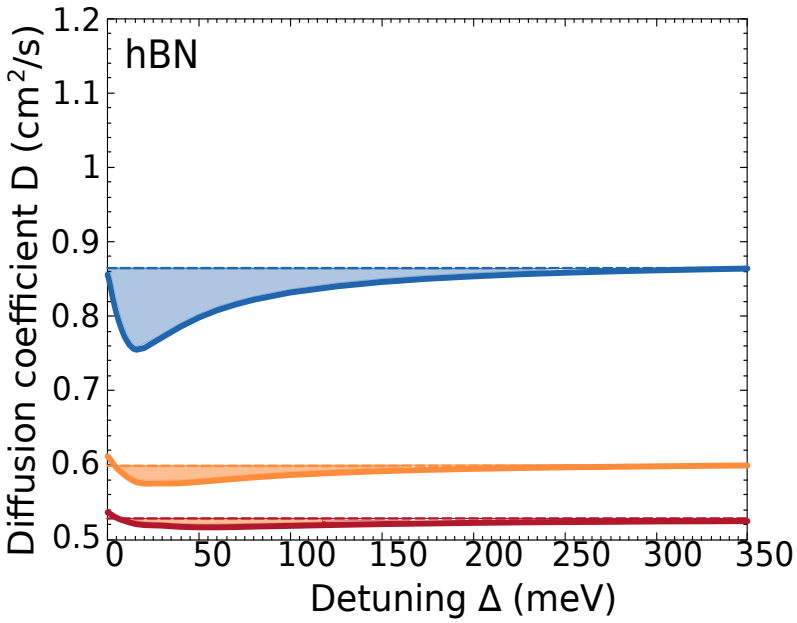

Figure 6.6: Diffusion coefficient for a monolayer of MoSe2 with hBN encapsulation.

7
Conclusion and Prospects

In this thesis we introduced the concept of the intervalley Coulomb exchange coupling in TMDs. The exchange coupling results in an exact superposition of the K and K' valleys, which is expressed by a two-branched band structure, which is Dirac-like at low momenta and parabolic in the limit of large momentum. Besides, we showed how a magnetic field can counteract the exchange coupling until the valleys are effectively decoupled and the band structure becomes parabolic. Secondly, we introduced phonons to the system and studied the influence of the exchange coupling on the exciton-phonon scattering. We found that the exciton-phonon coupling is modulated by a phase-dependent factor which has a large impact on scattering. By calculating the phonon assisted scattering rates, it became clear that the modification of the band structure gives rise to new scattering channels. Further, it has been shown that the scattering rates are magnetic field-dependent. Starting at a rate lower or comparable to the uncoupled case, they increase with small detuning due to the lifting of the phase-dependence. A point is then reached at which this effect is negligible and the decreasing number of states, due to the deforming band structure, takes over. In this regime, the scattering rate decreases with detuning until it is equal to the uncoupled case. Lastly, the excitonic diffusion coefficient was calculated. Here we predict that the diffusion coefficient should change in function of a magnetic field, which is not the case for a parabolic band structure. Due to the modified group velocity and the magnetic field dependence of the scattering rates, the diffusion coefficient knows a large increase at zero detuning, after which it drops below the uncoupled case. This is a direct consequence of the increasing scattering rates. When the latter starts decreasing, the diffusion coefficient increases until constant and equal to the uncoupled case. In future works it would be interesting to verify this phenomenon experimentally. This can be done by either measuring the diffusion coefficient or spectral broadening of MoSe2 under excitation with linearly polarised light.

Bibliography

[1] Roscoe G. Dickinson and Linus Pauling. "The crystal structure of molybdenite". In: *Journal of the American Chemical Society* 45.6 (1923), pp. 1466–1471.

[2] S. Lebègue and O. Eriksson. "Electronic structure of two-dimensional crystals from ab initio theory". In: *Phys. Rev. B* 79 (11 Mar. 2009), p. 115409.

[3] Wang Yao, Di Xiao, and Qian Niu. "Valley-dependent optoelectronics from inversion symmetry breaking". In: *Phys. Rev. B* 77 (23 June 2008), p. 235406.

[4] Di Xiao et al. "Coupled Spin and Valley Physics in Monolayers of MoS_2 and Other Group-VI Dichalcogenides". In: *Phys. Rev. Lett.* 108 (19 May 2012), p. 196802.

[5] Gui-Bin Liu et al. "Electronic structures and theoretical modelling of two-dimensional group-VIB transition metal dichalcogenides". In: *Chem. Soc. Rev.* 44 (9 2015), pp. 2643–2663.

[6] Hongyi Yu et al. "Valley excitons in two-dimensional semiconductors". In: *National Science Review* 2.1 (Jan. 2015), pp. 57–70.

[7] Hongyi Yu et al. "Dirac cones and Dirac saddle points of bright excitons in monolayer transition metal dichalcogenides". In: *Nature Communications* 5.1 (May 2014).

[8] Yuli V. Nazarov and Jeroen Danon. *Advanced Quantum Mechanics: A Practical Guide*. Cambridge University Press, 2013.

[9] Ermin Malic and Andreas Knorr. *Graphene and Carbon Nanotubes*. Wiley, 2013.

[10] Malte Selig. "Exciton-phonon coupling in monolayers of transition metal dichalcogenides". Doctoral Thesis. Berlin: Technische Universität Berlin, 2018.

[11] Hartmut Haug and Stephan W. Koch. *Quantum Theory of the Optical and Electronic Properties of Semiconductors*. 5th. WORLD SCIENTIFIC, 2009.

[12] Samuel Brem. "Microscopic Mechanisms of the Formation, Relaxation and Recombination of Excitons in Two-Dimensional Semiconductors". PhD thesis. Chalmers Tekniska Hogskola (Sweden), 2019.

[13] Zhenghe Jin et al. "Intrinsic transport properties of electrons and holes in monolayer transition-metal dichalcogenides". In: *Phys. Rev. B* 90 (4 July 2014), p. 045422.

[14] Xiaodong Li et al. "Intrinsic electrical transport properties of monolayer silicene and MoS2 from first principles". In: *Physical Review B* 87.11 (Mar. 2013).

[15] L. V. Keldysh. "Coulomb interaction in thin semiconductor and semimetal films". In: *Soviet Journal of Experimental and Theoretical Physics Letters* 29 (June 1979), p. 658.

[16] N. S. Rytova. “The screened potential of a point charge in a thin film”. In: *Moscow University Physics Bulletin* 3.3 (1967), p. 18.

[17] Diana Y. Qiu, Ting Cao, and Steven G. Louie. “Nonanalyticity, Valley Quantum Phases, and Lightlike Exciton Dispersion in Monolayer Transition Metal Dichalcogenides: Theory and First-Principles Calculations”. In: *Phys. Rev. Lett.* 115 (17 Oct. 2015), p. 176801.

[18] E. Wigner. “On the Quantum Correction For Thermodynamic Equilibrium”. In: *Phys. Rev.* 40 (5 June 1932), pp. 749–759.

[19] David K Ferry and Mihail Nedjalkov. *The Wigner Function in Science and Technology*. 2053-2563. IOP Publishing, 2018.

[20] Fausto Rossi and Tilmann Kuhn. “Theory of ultrafast phenomena in photoexcited semiconductors”. In: *Rev. Mod. Phys.* 74 (3 Aug. 2002), pp. 895–950.

[21] Ortwin Hess and Tilmann Kuhn. “Maxwell-Bloch equations for spatially inhomogeneous semiconductor lasers. I. Theoretical formulation”. In: *Phys. Rev. A* 54 (4 Oct. 1996), pp. 3347–3359.

[22] Roberto Rosati et al. “Negative effective excitonic diffusion in monolayer transition metal dichalcogenides”. In: *Nanoscale* 12 (1 2020), pp. 356–363.

A

Exchange Coupling Element

A.1 Excitonic Hamiltonian

Here follows a derivation of the exchange coupling element according to Yu et. al. [7]. We start with the exchange Hamiltonian:

$$\hat{H}_{ex} = \sum_{\mathbf{k},\mathbf{k}',\mathbf{q}} \mathcal{J}_{ex}(\mathbf{k},\mathbf{k}',\mathbf{q}) c^{\dagger K}_{\mathbf{k}+\mathbf{q}} v^{\dagger K'}_{\mathbf{k}'-\mathbf{q}} c^{K'}_{\mathbf{k}'} v^{K}_{\mathbf{k}} \tag{A.1}$$

where the matrix element $\mathcal{J}_{ex}$ is defined as

$$\mathcal{J}_{ex} = \int d\mathbf{r}_1 d\mathbf{r}_2 \psi^{\dagger cK}_{\mathbf{k}+\mathbf{q}}(\mathbf{r}_1) \psi^{\dagger vK'}_{\mathbf{k}'-\mathbf{q}}(\mathbf{r}_2) V(\mathbf{r}_1-\mathbf{r}_2) \psi^{cK'}_{\mathbf{k}'}(\mathbf{r}_2) \psi^{vK}_{\mathbf{k}}(\mathbf{r}_1), \tag{A.2}$$

with $V(\mathbf{r}_1-\mathbf{r}_2)$ the Coulomb potential. Note that due to spin-valley locking, spin is implicitly included in the Hamiltonian by the valley-index. We use Bloch waves to describe the electronic wave functions, thus defined as

$$\psi^{c/vK}_{\mathbf{q}}(\mathbf{r}) = \frac{1}{\sqrt{A}} e^{i(\mathbf{K}+\mathbf{q})\cdot\mathbf{r}} u^{c/vK}_{\mathbf{q}}(\mathbf{r}) \tag{A.3}$$

$$\psi^{c/vK'}_{\mathbf{q}}(\mathbf{r}) = \frac{1}{\sqrt{A}} e^{i(\mathbf{K}'+\mathbf{q})\cdot\mathbf{r}} u^{c/vK'}_{\mathbf{q}}(\mathbf{r}) \tag{A.4}$$

where A denotes the area of the 2D sheet. Now, we develop the Coulomb potential in its Fourier transform using $V(\mathbf{r}) = \sum_{\mathbf{p}} e^{i(\mathbf{p}\cdot\mathbf{r})} \frac{V(\mathbf{p})}{A}$:

$$\mathcal{J}_{ex} = \sum_{\mathbf{p}} \frac{V(\mathbf{p})}{A} \int d\mathbf{r}_1 d\mathbf{r}_2 \psi^{\dagger cK}_{\mathbf{k}+\mathbf{q}}(\mathbf{r}_1) \psi^{\dagger vK'}_{\mathbf{k}'-\mathbf{q}}(\mathbf{r}_2) e^{i(\mathbf{p}\cdot(\mathbf{r}_1-\mathbf{r}_2)} \psi^{cK'}_{\mathbf{k}'}(\mathbf{r}_2) \psi^{vK}_{\mathbf{k}}(\mathbf{r}_1), \tag{A.5}$$

Inserting the Bloch waves from equations A.3 and A.4 and separating the integrals, we get:

$$\mathcal{J}_{ex} = \sum_{\mathbf{p}} \frac{V(\mathbf{p})}{A} \frac{1}{A} \int d\mathbf{r}_1 u^{\dagger cK}_{\mathbf{k}+\mathbf{q}}(\mathbf{r}_1) e^{i(\mathbf{p}+\mathbf{q})\cdot\mathbf{r}_1} u^{vK}_{\mathbf{k}}(\mathbf{r}_1) \frac{1}{A} \int d\mathbf{r}_2 u^{\dagger vK'}_{\mathbf{k}'-\mathbf{q}}(\mathbf{r}_2) e^{-i(\mathbf{p}+\mathbf{q})\cdot\mathbf{r}_2} u^{cK'}_{\mathbf{k}'}(\mathbf{r}_2) \tag{A.6}$$

The integration over space can be subdivided in integrals over the unit cell, i.e. setting $\mathbf{r} = \mathbf{R}_n + \mathbf{r}_n$, with $\mathbf{R}_n$ the lattice vector and $\mathbf{r}_n$ the space vector in the unit cell, and summing over $\mathbf{R}_n$. Using the translation symmetry of the Bloch factors one obtains:

$$\begin{aligned}\mathcal{J}_{ex} = \sum_{\mathbf{p}} \frac{V(\mathbf{p})}{A} \sum_{\mathbf{R}_n^1} e^{i(\mathbf{p}+\mathbf{q})\cdot\mathbf{R}_n^1} \frac{1}{A} \int_{UC} d\mathbf{r}_n^1 u_{\mathbf{k}+\mathbf{q}}^{\dagger cK}(\mathbf{r}_n^1) e^{i(\mathbf{p}+\mathbf{q})\cdot\mathbf{r}_n^1} u_{\mathbf{k}}^{vK}\mathbf{r}_n^1) \\ \times \sum_{\mathbf{R}_n^2} e^{-i(\mathbf{p}+\mathbf{q})\cdot\mathbf{R}_n^2} \frac{1}{A} \int_{UC} d\mathbf{r}_n^2 u_{\mathbf{k}'-\mathbf{q}}^{\dagger vK'}(\mathbf{r}_n^2) e^{-i(\mathbf{p}+\mathbf{q})\cdot\mathbf{r}_n^2} u_{\mathbf{k}'}^{cK'}(\mathbf{r}_n^2)\end{aligned} \tag{A.7}$$

A useful property of the lattice vectors (without derivation) is $\sum_{\mathbf{R}_n} e^{\mathbf{q}\cdot\mathbf{R}_n} = N \sum_{\mathbf{G}} \delta_{\mathbf{G},\mathbf{q}}$, with $\mathbf{G}$ the reciprocal lattice vector and N the number of unit cells. Using this identity to convert the sums over $\mathbf{R}_n$, results in:

$$\begin{aligned}\mathcal{J}_{ex} = \sum_{\mathbf{G}} \frac{V(\mathbf{G}-\mathbf{q})}{A} \frac{N}{A} \int_{UC} d\mathbf{r}^1 u_{\mathbf{k}+\mathbf{q}}^{\dagger cK}(\mathbf{r}^1) e^{i\mathbf{G}\cdot\mathbf{r}^1} u_{\mathbf{k}}^{vK}\mathbf{r}^1) \\ \times \frac{N}{A} \int_{UC} d\mathbf{r}^2 u_{\mathbf{k}'-\mathbf{q}}^{\dagger vK'}(\mathbf{r}^2) e^{-i\mathbf{G}\cdot\mathbf{r}^2} u_{\mathbf{k}'}^{cK'}(\mathbf{r}^2)\end{aligned} \tag{A.8}$$

Lastly, recognising the integrals as inner products of the Bloch factors, we can write

$$\mathcal{J}_{ex} = \sum_{\mathbf{G}} \frac{V(\mathbf{G}-\mathbf{q})}{A} \left\langle u_{\mathbf{k}+\mathbf{q}}^{cK} \right| e^{i\mathbf{G}\cdot\mathbf{r}} \left| u_{\mathbf{k}}^{vK} \right\rangle \left\langle u_{\mathbf{k}'-\mathbf{q}}^{vK'} \right| e^{-i\mathbf{G}\cdot\mathbf{r}} \left| u_{\mathbf{k}'}^{cK'} \right\rangle \tag{A.9}$$

The next step in the derivation is to transform the Hamiltonian into excitonic basis. Using the fundamental anti-commutation relations, the Hamiltonian can be rewritten into

$$\hat{H}_{ex} = \sum_{\mathbf{k},\mathbf{k}',\mathbf{q}} \mathcal{J}_{ex}(\mathbf{k},\mathbf{k}',\mathbf{q}) c_{\mathbf{k}+\mathbf{q}}^{\dagger K} v_{\mathbf{k}}^{K} v_{\mathbf{k}'-\mathbf{q}}^{\dagger K'} c_{\mathbf{k}'}^{K'} \tag{A.10}$$

Now we introduce pair operators $A_{\mathbf{k}_c,\mathbf{k}_v}^{\dagger\xi}, A_{\mathbf{k}_c,\mathbf{k}_v}^{\xi}$ in valley $\xi = K/K'$, defined as

$$A_{\mathbf{k}_c,\mathbf{k}_v}^{\dagger\xi} = c_{\mathbf{k}_c}^{\dagger\xi} v_{\mathbf{k}_v}^{\xi} \tag{A.11}$$

$$A_{\mathbf{k}_c,\mathbf{k}_v}^{\dagger\xi} = v_{\mathbf{k}_v}^{\dagger\xi} c_{\mathbf{k}_c}^{\xi} \tag{A.12}$$

These can be identified in the Hamiltonian, resulting in

$$\hat{H}_{ex} = \sum_{\mathbf{k},\mathbf{k}',\mathbf{q}} \mathcal{J}_{ex}(\mathbf{k},\mathbf{k}',\mathbf{q}) A_{\mathbf{k}+\mathbf{q},\mathbf{k}}^{\dagger K} A_{\mathbf{k}'-\mathbf{q},\mathbf{k}'}^{K'} \tag{A.13}$$

In order to go to excitonic basis, the Hamiltonian needs to be written in a joint coordinate system for electrons and holes. Therefore we introduce the centre-of-mass momentum $\mathbf{Q}$ and relative momentum $\mathbf{q}$ as

$$\mathbf{Q} = \mathbf{k}_c - \mathbf{k}_v \tag{A.14}$$

$$\mathbf{q} = \frac{m_v}{m_v + m_c}\mathbf{k}_v + \frac{m_c}{m_v + m_c}\mathbf{k}_c \tag{A.15}$$

with m_c/v the mass of an electron in the conduction/valence band. In these coordinates, the Hamiltonian reads

$$\hat{H}_{ex} = \sum_{\mathbf{Q},\mathbf{q},\mathbf{q'}} \mathcal{J}_{ex}(\mathbf{Q},\mathbf{q},\mathbf{q}') A^{\dagger K}_{\mathbf{q}-\frac{\mathbf{Q}}{2},\mathbf{q}+\frac{\mathbf{Q}}{2}} A^{K'}_{\mathbf{q}'+\frac{\mathbf{Q}}{2},\mathbf{q}'-\frac{\mathbf{Q}}{2}} \tag{A.16}$$

where the approximation was made that $m_c \approx m_v$. Note also that the relative vector **q,q'** are the relative vectors, not to be confused with the momentum transfer **q** in the Hamiltonian. Now we can develop the pair operators into excitonic eigenmodes using the excitonic wave functions $\psi(\mathbf{q})$:

$$A^{\dagger\xi}_{\mathbf{q}+\frac{\mathbf{Q}}{2},\mathbf{q}-\frac{\mathbf{Q}}{2}} = \psi(\mathbf{q}) X^{\dagger\xi}_{\mathbf{Q}} \tag{A.17}$$

$$\tag{A.18}$$

where $\{X^{\dagger\xi}_{\mathbf{Q}}, X^{\xi}_{\mathbf{Q}}\}$ are excitonic operators, creating/destroying an exciton with momentum $\mathbf{Q}$ in valley ξ. The transformed Hamiltonian becomes

$$\hat{H}_{ex} = \mathcal{J}_{\mathbf{Q}} X^{\dagger K}_{\mathbf{Q}} X^{K'}_{\mathbf{Q}} + \text{h.c.} \tag{A.19}$$

The transformed exchange coupling reads

$$\mathcal{J}_{\mathbf{Q}} = \sum_{\mathbf{q}\mathbf{q}'} \psi(\mathbf{q})\psi(-\mathbf{q}')\mathcal{J}_{ex}(\mathbf{Q},\mathbf{q},\mathbf{q}') \tag{A.20}$$

$$\begin{aligned} &= \sum_{\mathbf{Q}} \frac{V(\mathbf{G}+\mathbf{Q})}{A} \left(\sum_{q} \psi(\mathbf{q}) \left\langle u^{cK}_{\mathbf{q}+\frac{\mathbf{Q}}{2}} \right| e^{i\mathbf{G}\cdot\mathbf{r}} \left| u^{vK}_{\mathbf{q}-\frac{\mathbf{Q}}{2}} \right\rangle \right) \\ &\times \left(\sum_{\mathbf{q}'} \psi(-\mathbf{q}') \left\langle \mathbf{u}^{\mathbf{vK}'}_{\mathbf{q}'-\frac{\mathbf{Q}}{2}} \right| \mathbf{e}^{-\mathbf{iG}\cdot\mathbf{r}} \left| \mathbf{u}^{\mathbf{cK}'}_{\mathbf{q}'+\frac{\mathbf{Q}}{2}} \right\rangle \right) \end{aligned} \tag{A.21}$$

A.2 Expression for the exchange coupling

The sum over **G** can be split into a long-range part (**G**=0) and a short-range part (**G**≠0). Because we treat Wannier excitons, which are limited in momentum space, nd for symmetry reasons, the short range part can be neglected:

$$\mathcal{J}_{\mathbf{Q}} = \sum_{\mathbf{Q}} \frac{V(\mathbf{Q})}{A} \left(\sum_{q} \psi(\mathbf{q}) \left\langle u^{cK}_{\mathbf{q}+\frac{\mathbf{Q}}{2}} \middle| u^{vK}_{\mathbf{q}-\frac{\mathbf{Q}}{2}} \right\rangle \right) \left(\sum_{\mathbf{q}'} \psi(-\mathbf{q}') \left\langle \mathbf{u}^{\mathbf{vK}'}_{\mathbf{q}'-\frac{\mathbf{Q}}{2}} \middle| \mathbf{u}^{\mathbf{cK}'}_{\mathbf{q}'+\frac{\mathbf{Q}}{2}} \right\rangle \right) \tag{A.22}$$

In order to proceed, one needs to use a $\mathbf{k}\cdot\mathbf{p}$ expansion [11] for the matrix element $\left\langle u^{cK}_{\mathbf{q}+\frac{\mathbf{Q}}{2}} \middle| u^{vK}_{\mathbf{q}-\frac{\mathbf{Q}}{2}} \right\rangle$:

$$\left| u^{cK}_{\mathbf{q}+\frac{\mathbf{Q}}{2}} \right\rangle = \left| u^{cK}_{\mathbf{q}} \right\rangle + \frac{\hbar}{2m}\mathbf{Q}\cdot\frac{\left\langle u^{vK}_{\mathbf{q}} \right| \hat{\mathbf{p}} \left| u^{cK}_{\mathbf{q}} \right\rangle}{E^{cK}_{\mathbf{q}} - E^{vK}_{\mathbf{q}}} \left| u^{vK}_{\mathbf{q}} \right\rangle + \mathcal{O}(\mathbf{Q}^2) \tag{A.23}$$

$$\left| u^{vK}_{\mathbf{q}-\frac{\mathbf{Q}}{2}} \right\rangle = \left| u^{vK}_{\mathbf{q}} \right\rangle + \frac{\hbar}{2m}\mathbf{Q}\cdot\frac{\left\langle u^{vK}_{\mathbf{q}} \right| \hat{\mathbf{p}} \left| u^{vK}_{\mathbf{q}} \right\rangle}{E^{vK}_{\mathbf{q}} - E^{cK}_{\mathbf{q}}} \left| u^{cK}_{\mathbf{q}} \right\rangle + \mathcal{O}(\mathbf{Q}^2) \tag{A.24}$$

Inserting this in the equation gives:

$$\left\langle u^{cK}_{\mathbf{q}+\frac{\mathbf{Q}}{2}} \middle| u^{vK}_{\mathbf{q}-\frac{\mathbf{Q}}{2}} \right\rangle = \frac{\hbar}{m}\mathbf{Q}\cdot\frac{\left\langle u^{cK}_{\mathbf{q}}\middle|\,\hat{\mathbf{p}}\,\middle|u^{vK}_{\mathbf{q}}\right\rangle}{E^{cK}_{\mathbf{q}-E^{vK}_{\mathbf{q}}}} + \mathcal{O}(\mathbf{Q}^2) \tag{A.25}$$

Note that because we consider small wave vectors, it is sufficient to go up to first order in $\mathbf{Q}$. In equation A.25 one can recognise the expression for the optical dipole matrix element [11]:

$$\mathbf{d}^{cv\xi}_{\mathbf{q}} = \frac{i\hbar}{m}\mathbf{Q}\cdot\frac{\left\langle u^{c\xi}_{\mathbf{q}}\middle|\,\hat{\mathbf{p}}\,\middle|u^{v\xi}_{\mathbf{q}}\right\rangle}{E^{c\xi}_{\mathbf{q}} - E^{v\xi}_{\mathbf{q}}} \tag{A.26}$$

Doing similar for the factor in A.22, one obtains

$$\mathcal{J}_{\mathbf{Q}} = V(\mathbf{Q})(\mathbf{Q}\cdot\mathbf{d}^{K}_{X_0})(\mathbf{Q}\cdot\mathbf{d}^{*K'}_{X_0}) \tag{A.27}$$

where the excitonic optical matrix elements are defined as $\mathbf{d}^{K}_{X_0} = \frac{1}{\sqrt{A}}\sum_{\mathbf{q}}\psi(\mathbf{q})\mathbf{d}^{cvK}_{\mathbf{q}}$, $\mathbf{d}^{K'}_{X_0} = \frac{1}{\sqrt{A}}\sum_{\mathbf{q}'}\psi^*(-\mathbf{q}')\mathbf{d}^{cvK}_{\mathbf{q}'}$. Now the valley optical selection rules become important. Because the K (K') valley only couples to $\sigma+$ ($\sigma-$) polarised light, the optical matrix element must take the form of the corresponding Jones vectors s.t. $\mathbf{d}^{K}_{X_0} = (d^{Kx}_{X_0}, d^{Ky}_{X_0}) = (d^{Kx}_{X_0}, -id^{Kx}_{X_0})$ and $\mathbf{d}^{K'}_{X_0} = (d^{K'x}_{X_0}, id^{K'x}_{X_0})$. Furthermore, due to rotational symmetry of the K/K' points and hence the band structure, the centre-of-mass momentum is circularly symmetric, s.t. $\mathbf{Q} = (Q_x, Q_Y) = (Q\cos\theta, Q\sin\theta)$. Thus, the exchange coupling get the form

$$\mathcal{J}_{\mathbf{Q}} = V(\mathbf{Q})Q^2(d^{xK}_{X_0})^2 e^{-2i\theta} \tag{A.28}$$

Because we treat Wannier excitons, the extend in momentum space is small. Therefore, neglecting the momentum dependence of the non-transformed optical matrix element, we get $\mathbf{d}^{K}_{X_0} \approx \frac{\mathbf{d}^{cvK}}{\sqrt{A}}\sum_{\mathbf{q}}\psi(\mathbf{q})$. The previous definition of the optical matrix element simplifies to $\mathbf{d}^{cvK} = \frac{i\hbar}{m}\frac{\left\langle u^{cK}\middle|\hat{\mathbf{p}}\middle|u^{vK}\right\rangle}{E_g}$, with E_g the gap energy. Comparing to the optical matrix element in [**opticalselectionrules**], one obtains $\mathbf{d}^{cvK} = (i\frac{at}{E_g}, \frac{at}{E_g})$, with a the in-plane lattice constant of the monolayer and t the hopping amplitude. Finally one arrives at the final expression

$$\mathcal{J}_{\mathbf{Q}} = -\frac{|\sum_{\mathbf{q}}\psi(\mathbf{q})|^2}{A}\frac{a^2t^2}{E_g^2}V(\mathbf{Q})Q^2e^{-2i\theta} \tag{A.29}$$

B

Material Parameters MoSe2

Table B.1: Table with materials parameters used in this thesis. Sources: hopping parameter [4], rest see [10]

lattice	a_0 [nm]	d_0 [nm]	$\epsilon_\perp$	$\epsilon_\parallel$	t
	0.31854	0.64	16.5	7.4	0.94

electrons	m_c $[m_0]$	m_v $[m_0]$	E_g [eV]		
	0.6	0.5	1.928		

.

acoustic phonons	v_{ph} [nm/fs]	$\|D^v\|$ [eV]	$\|D^c\|$ [eV]		
	4.1e-3	2.8	3.4		

optical phonons	Ω^{LO}[eV]	Ω^{TO}[eV]	Ω^{A_1} [eV]	$\|D^v\|$[eV/nm]	$\|D^c\|$[eV/nm]
	0.0361	0.0366	0.0303	49	52